Available online at www.sciencedirect.com

ScienceDirect

Advances in Space Research 77 (2026) 12096–12121

ADVANCES IN SPACE RESEARCH (a COSPAR publication)

www.elsevier.com/locate/asr

Joint optimization of a GRACE radiation pressure model, the accelerometer scale factors, and an empirical magnetic-field-induced accelerometer bias

F. Jacobs *, N. Hładczuk, J. van den IJssel, C. Siemes, P. Visser

Astrodynamics and Space Missions Section, Faculty of Aerospace Engineering, Delft University of Technology, Kluyverweg 1, Delft 2629 HS, the Netherlands

Received 13 February 2026; received in revised form 7 April 2026; accepted 9 April 2026
Available online 16 April 2026

Abstract

Valuable insights into the thermospheric mass density and horizontal winds can be obtained from satellites equipped with accelerometers. To derive these quantities, radiation pressure must be accurately modeled and removed from the calibrated accelerometer measurements. However, the documented surface reflection and absorption coefficients, as well as the satellite's thermal properties, are often inaccurate or, in some cases, even absent. This study presents a method for optimizing these parameters jointly with the accelerometer scale factors. Focusing on GRACE data from 2009, a case where radiation pressure was dominant over aerodynamic force, enabled us to refine the radiation pressure model without detrimental effects from errors in aerodynamic force modeling. We evaluated three variants of estimating the scale factor: estimating no accelerometer scale factors, only the y-axis scale factor, or both the y- and z-axis scale factors. We use the difference between the measured and modeled accelerations (the residual) as our target functional. Estimating both scale factors yielded the lowest residual for both GRACE satellites, even though the radiation pressure model was tuned using GRACE-A data only. After the optimization, we observed a systematic feature in the cross-track residuals within the geographical domain, which strongly correlates with the magnetic field vector experienced by the spacecraft. While its cause remains unknown, we introduced an empirical correction that effectively removed the feature and significantly increased consistency between GRACE-A and GRACE-B. Overall, we were able to reduce the RMS of the residuals by more than 13% in the cross-track direction and 32% in the radial direction, indicating a significant increase in modeling accuracy. The presented method provides a generalizable approach that can also be applied to future satellite missions with accelerometers.

Keywords: GRACE; Accelerometer scale factors; Radiation pressure modeling; Magnetic-field-induced accelerometer bias

1. Introduction

Satellites equipped with accelerometers help to improve our understanding of the upper atmosphere. From their measurements, thermosphere mass density and crosswind observations can be inferred (Doornbos et al., 2010). These observations are essential for improving empirical thermosphere models, such as the Drag Temperature Model (DTM) (Bruinsma and Boniface, 2021). One of the missions used for this purpose is the Gravity Recovery and Climate Experiment (GRACE) mission (Tapley et al., 2004). GRACE aims to measure Earth's time-variable gravity field by precisely tracking the distance between two satellites, GRACE-A and GRACE-B. The accelerometers measure the non-gravitational acceleration acting on each

* Corresponding author.
E-mail address: f.jacobs@tudelft.nl (F. Jacobs).

https://doi.org/10.1016/j.asr.2026.04.043

satellite, allowing its effect on the ranging measurements to be accounted for when retrieving gravity field models. The satellites flew initially at approximately 500 km altitude with an inclination of 89.5°. They were in the same orbital plane, separated only by approximately 220 km or 29 s, which means that they experience a very similar environment from a force modeling perspective. The mission ended in 2017, and both satellites have meanwhile reentered.

To extract the aerodynamic acceleration from the GRACE accelerometer data, all other accelerations must be removed, with thruster firings and radiation pressure being the primary remaining effects. Thruster activations are typically short and discrete, and can be excluded using onboard telemetry. Radiation pressure, however, is continuous and must be modeled explicitly. It arises from three sources: direct solar radiation, Earth-reflected and emitted radiation (albedo and infrared), and thermal emission from the satellite itself. State-of-the-art radiation pressure models utilize ray-tracing, along with thermal inertia modeling, to simulate the acceleration due to radiation pressure (Hładczuk et al., 2024). The ray-tracing component depends on surface reflection and absorption coefficients, while the thermal model relies on panel-specific heat absorption and thermal capacity. The radiation pressure model parameters often stem from models for spacecraft thermal control and lack the accuracy required for accurate radiation pressure modeling.

For the GRACE mission, nominal surface coefficients are provided in the Data Product User Handbook of GRACE-FO (Wen et al., 2019), but their accuracy remains uncertain. Furthermore, due to surface degradation, the coefficients might change while in orbit. Manual tuning of the reflection and absorption coefficients has been performed by Siemes et al. (2023). Later, Hładczuk et al. (2024) demonstrated an optimization method for estimating surface properties from satellite accelerometer measurements for GRACE-FO. However, a similar step has not yet been taken for GRACE. In this work, the science reference frame (SRF) is used to define the x-, y-, and z-axis. The x-, y-, and z-axes are approximately aligned with the along-track, cross-track, and nadir directions, respectively. One of the important assumptions in previous work is that the accelerometer's scale factors are correct. The scale factors and biases are typically determined using precise orbit determination (POD). However, it has been previously shown that the POD method exhibits shortcomings in the y- and z-axes (Siemes et al., 2023; Wöske et al., 2024). Therefore, they suggest using non-conservative force models to recalibrate the bias for those axes. However, this is not done for the scale factor for those axes, while it may encounter the same issues. A comparison between calibration coefficients using either POD or non-gravitational force modeling has been adopted, e.g., by Koch et al. (2018). They showed that the scale factors obtained by non-gravitational force modeling depend on the surface properties and the selected aerodynamic model.

Overall, the goal of this paper is to enhance the quality of thermospheric density and wind data by developing a highly accurate radiation pressure model and optimizing accelerometer calibration. Therefore, we present an extension to the radiation pressure model tuning method proposed by Hładczuk et al. (2024), which was applied to GRACE-FO. Overall, we aim to minimize the residual acceleration between the modeled and measured acceleration. Firstly, the presented method jointly optimizes the absorption and reflection coefficients, as well as thermal model parameters, for the GRACE satellites. Additionally, it estimates the accelerometer scale factors for the y- and/or z-axes. In the second part of the paper, an empirical magnetic-field-induced accelerometer bias will also be introduced to reduce the residual between modeled and measured acceleration even more. We use accelerometer data from 2009, which is characterized by low solar (mean $F10.7 = 70\text{sfu}$[1]) and geomagnetic activity (mean $A_p = 4$[2]), resulting in low density and winds at the altitude of the GRACE satellites (≈ 467 km). Consequently, radiation pressure dominates over aerodynamic forces during that period, allowing us to accurately isolate the radiation pressure acceleration from the accelerometer data and refine the radiation pressure model parameters. This approach enables an independent tuning of the radiation pressure model, improving the separation between radiation-induced and aerodynamic accelerations and thereby enhancing the reliability of thermosphere density and cross-wind observations. Although surfaces slowly degrade in the harsh space environment, their properties are not expected to change much over time, and the tuned radiation pressure model is assumed to be valid throughout the mission.

The remainder of this paper is structured as follows. First, we outline the methodology of the accelerometer calibration, non-conservative force modeling, and optimization in Section 2. Afterwards, we give an overview of the data used within this work in Section 3. In Section 4, we present a step-by-step analysis of how the joint optimization of accelerometer scale factors, along with the radiation pressure model, improves modeling accuracy. Based on remaining residuals, we expand the optimization space in Section 5, taking into account infrared reflection and absorption coefficients for the nadir panel as well as a magnetic-field-induced accelerometer bias in the cross-track direction. Using the fine-tuned radiation pressure model, accelerometer scale factors, and magnetic-field-induced bias corrections, Section 6 demonstrates the improvements achieved in accelerometer-derived crosswind observations. Finally, we draw conclusions in Section 7 and provide an outlook to future work in Section 8.

[1] Retrieved from https://www.ngdc.noaa.gov/stp/space-weather/swpc-products/annual_reports/daily_solar_indices_summaries/daily_solar_data/

[2] Retrieved from https://www.ngdc.noaa.gov/stp/space-weather/swpc-products/annual_reports/daily_solar_indices_summaries/daily_geomagnetic_data/

2. Methodology

The accelerometers of GRACE are precisely located at the satellite center of mass, which is actively maintained by adjusting trim masses (Wang, 2003). This enables the accelerometers to measure the non-gravitational linear acceleration acting on the satellites directly. However, the accelerometer data require calibration before they can be used. Therefore, a bias vector $\boldsymbol{b}$ and a diagonal scale factor matrix $\boldsymbol{S}$ are applied to the measured accelerations $\boldsymbol{a}_{\text{meas}}$ to obtain the calibrated acceleration

$$\boldsymbol{a}_{\text{cal}} = \boldsymbol{S}\boldsymbol{a}_{\text{meas}} + \boldsymbol{b}. \tag{1}$$

Typically, the scale factors and biases are determined by precise orbit determination (POD) (Helleputte et al., 2009). Cross-talk between the accelerometer axes is not accounted for because it is difficult to estimate via POD (Siemes et al., 2023; Wöske et al., 2024).

The non-gravitational accelerations can also be modeled as the sum of the external radiation pressure acceleration $\boldsymbol{a}_{\text{rad}}$, the heat emission acceleration $\boldsymbol{a}_{\text{he}}$, the aerodynamic acceleration $\boldsymbol{a}_{\text{aero}}$, and the acceleration $\boldsymbol{a}_{\text{thrust}}$ caused by thruster activations, i.e. the modeled acceleration is

$$\boldsymbol{a}_{\text{mod}} = \boldsymbol{a}_{\text{rad}} + \boldsymbol{a}_{\text{he}} + \boldsymbol{a}_{\text{aero}} + \boldsymbol{a}_{\text{thrust}}. \tag{2}$$

Within this work, we simplify Eq. (2) by considering only the radiation and aerodynamic contributions, whereas acceleration data affected by thruster activations are excluded from our analysis. The latter is possible because the thrusters are activated only occasionally in short pulses. Since a windowed filter of 70.7 s is used for the conversion from Level 1A to Level 1B data (Case et al., 2010), a thruster activation's footprint extends up to 35 s before and after the thruster firing. To ensure that the thruster activations have no impact on our results, we exclude all acceleration data within this footprint, which corresponds to approximately 28 % of the data. Thus, we omit $\boldsymbol{a}_{\text{thrust}}$ in the following.

Since both the modeled and calibrated accelerations represent the non-gravitational acceleration acting on the satellite, they should be equal. However, measurement noise, as well as calibration and modeling errors, cause discrepancies between them, reflected in the residual acceleration

$$\Delta\boldsymbol{a} = \boldsymbol{a}_{\text{mod}} - \boldsymbol{a}_{\text{cal}}. \tag{3}$$

The knowledge that the residual acceleration should be zero can be used to amend some of the calibration and modeling errors. Since the aerodynamic acceleration plays a central role in this context, we first explain how to calculate it.

The aerodynamic acceleration is modeled according to

$$\boldsymbol{a}_{\text{aero}} = \frac{1}{2}\frac{\rho}{m} v_{\text{rel}}^2 \boldsymbol{C}_{\text{aero}}, \tag{4}$$

where ρ is the thermospheric density, m the satellite mass, and $v_{\text{rel}} = |\,\boldsymbol{v}_{\text{rel}}\,|$ the magnitude of the velocity vector $\boldsymbol{v}_{\text{rel}}$ of the satellite relative to the surrounding atmosphere. The aerodynamic force coefficient vector $\boldsymbol{C}_{\text{aero}}$ is intrinsically multiplied by the cross-sectional area exposed to the atmospheric flow and accounts for drag, lift, and side forces, as well as self-shadowing effects (March et al., 2019).

To obtain the aerodynamic acceleration from Eq. (4), we require the density ρ. Thermosphere models have errors of 10–30% in density (Bruinsma et al., 2018), which are too large for our purposes. Moreover, using a thermosphere model would bias the estimation of surface properties toward that model, defeating the purpose of the density observations, which is to improve and validate thermosphere models. The only other option for accurately obtaining density is to derive it from the calibrated accelerometer measurements. In more detail, we replace $\boldsymbol{a}_{\text{mod}}$ by $\boldsymbol{a}_{\text{cal}}$ in Eq. (2) to obtain

$$\boldsymbol{a}_{\text{aero}} = \boldsymbol{a}_{\text{cal}} - \boldsymbol{a}_{\text{rad}} - \boldsymbol{a}_{\text{he}}, \tag{5}$$

reminding that we omit $\boldsymbol{a}_{\text{thrust}}$. Then, we derive the density by solving the x-axis component of Eq. (4) for the density, which gives

$$\rho = \frac{2ma_{\text{aero},x}}{C_{\text{aero},x} v_{\text{rel}}^2} = \frac{2m(a_{\text{cal},x} - a_{\text{rad},x})}{C_{\text{aero},x} v_{\text{rel}}^2}. \tag{6}$$

This approach is motivated by the fact that aerodynamic drag acts primarily in the x-direction, and because this direction can be accurately calibrated by POD (Siemes et al., 2023). Finally, we insert the expression for the density into Eq. (4) to obtain the aerodynamic acceleration. Note that due to the low density caused by low solar activity in 2009 and the high altitude of the GRACE satellites, the aerodynamic acceleration has only a minor contribution to the cross-track and radial directions, so the error in the obtained density has a negligible effect on those directions.

When calculating the aerodynamic acceleration in this way, the x-component of $\Delta\boldsymbol{a}$ is zero by definition. However, the y- and z-components still reflect calibration and modeling errors, which enabled Siemes et al. (2023) as well as Wöske et al. (2024) to estimate the y- and z-components of the accelerometer bias vector. In this work, however, we focus on estimating the parameters for the radiation pressure model and the accelerometer scale factors, rather than the accelerometer bias vector. Therefore, we describe the calculation of radiation pressure and the optimization method in the remainder of this section.

2.1. Radiation pressure acceleration

The radiation pressure acting upon the spacecraft has three sources: solar radiation, Earth's radiation, and the radiation emitted by the spacecraft itself. Solar radiation is strongest in the visible bandwidth, whereas Earth's radiation occurs in both the visible and infrared bandwidths, due to Earth's albedo and its emission of heat. Likewise, the satellite's radiation is caused by heat emission in the infrared bandwidth.

The solar and Earth's radiation pressures are calculated by

$$\boldsymbol{a}_{\mathrm{rad}} = \frac{\Phi_\lambda}{cm}\boldsymbol{C}_{\mathrm{rad},\lambda}, \tag{7}$$

where c is the speed of light, m the mass of the satellite, Φ_λ the radiation flux, and $\boldsymbol{C}_{\mathrm{rad},\lambda}$ the radiation pressure force coefficient vector, intrinsically multiplied with the satellite's cross-sectional area. The flux and the force coefficient are different for visible and infrared radiation, which we signify with the subscript $\lambda \in \{\mathrm{vis}, \mathrm{ir}\}$.

The force coefficients $\boldsymbol{C}_{\mathrm{rad},\lambda}$ are obtained through ray-tracing simulations, using a highly accurate satellite geometry model and accounting for self-shadowing and multiple reflections (Siemes et al., 2023). They can be expressed as a linear combination of the contributions from absorption (a), diffusive (d), and specular (s) reflection by each material i, i.e.

$$\boldsymbol{C}_{\mathrm{rad},\lambda} = \sum_i c_{\mathrm{a},\lambda,i}\boldsymbol{C}_{\mathrm{a},\lambda,i} + c_{\mathrm{d},\lambda,i}\boldsymbol{C}_{\mathrm{d},\lambda,i} + c_{\mathrm{s},\lambda,i}\boldsymbol{C}_{\mathrm{s},\lambda,i}, \tag{8}$$

where coefficient c_a specifies the fraction of absorbed radiation, while coefficients c_s and c_d are the fractions of specularly and diffusely reflected radiation, respectively.

The radiation pressure caused by the satellite's heat emission is calculated using the thermal model described in detail by Hładczuk et al. (2024), which accounts for the satellite's thermal inertia. Here, we highlight only the parts relevant to this work. The thermal model uses a panel representation of the satellite, where the rate of heat change

$$\dot{Q}_j = (1 - e_j)\dot{Q}_{\mathrm{a},j} - \dot{Q}_{\mathrm{e},j} - \dot{Q}_{\mathrm{c},j}, \tag{9}$$

is calculated for each panel j based on the contributions from the absorbed (a), emitted (e), and conducted (c) heat. Each panel is linked to the satellite body via a heat conduction coefficient. We assume, similar to Siemes et al. (2023), an internal heat generation of the body of 70 W and a heat capacity of 100 $\mathrm{kJ{\cdot}K^{-1}}$. For solar panels, part of the absorbed radiation is converted into electricity instead of heat. This is accounted for by the coefficient e_j, indicating the fraction of radiation converted to electricity. The temperature evolution of a panel can then be calculated by

$$T_j(t + \Delta t) = T_j(t) + \frac{\dot{Q}_j}{C_j}\Delta t, \tag{10}$$

where T_j is the panel temperature, t is the epoch, Δt is the time step, and C_j the heat capacity of the panel. The acceleration due to the satellite's heat emission is

$$\boldsymbol{a}_{\mathrm{he}} = -\frac{2}{3}\sum_j \frac{A_j\epsilon_j\sigma T_j^4}{mc}\boldsymbol{n}_j \tag{11}$$

in which $\epsilon_j = c_{\mathrm{a,ir},j}$ is the emissivity of the panel, σ is the Stefan–Boltzmann constant, and A_j and $\boldsymbol{n}_j$ are the panel's area and outward normal vector, respectively.

2.2. Optimization

As aforementioned, we aim to estimate the parameters of the radiation pressure model and the accelerometer scale factors. Therefore, we minimize the errors in the residual accelerations Δa_y and Δa_z. For that purpose, we define the objective function θ as

$$\theta = \sqrt{\Delta\boldsymbol{a}_y^T\Delta\boldsymbol{a}_y + \Delta\boldsymbol{a}_z^T\Delta\boldsymbol{a}_z}, \tag{12}$$

to be minimized as a function of corrections to the radiation pressure model and accelerometer scale factors. The vectors

$$\Delta\boldsymbol{a}_y = \begin{bmatrix}\Delta a_y(t_1)\\ \vdots \\ \Delta a_y(t_N)\end{bmatrix} \text{ and } \Delta\boldsymbol{a}_z = \begin{bmatrix}\Delta a_z(t_1)\\ \vdots \\ \Delta a_z(t_N)\end{bmatrix} \tag{13}$$

collect Δa_y and Δa_z for all epochs t_i. To maintain the computational effort manageable, Δa_y and Δa_z were sampled every $\Delta t = 10$ s, downsampling from the original 1 Hz accelerometer measurements. For optimization, we need the partial derivatives of Δa_y and Δa_z with respect to the radiation pressure model parameters and the scale factors, which we compute using a finite-difference approximation.

This approach to estimating corrections to the radiation pressure model is conceptually similar to the one by Hładczuk et al. (2024), who used only the residual acceleration $\Delta\boldsymbol{a}_y$, i.e. $\theta = \sqrt{\Delta\boldsymbol{a}_y^T\Delta\boldsymbol{a}_y}$ in their optimization. During our initial analysis, we observed that the error in the z-direction significantly increased when using only $\Delta\boldsymbol{a}_y$, which motivated us to expand the objective function such that also the error in $\Delta\boldsymbol{a}_z$ is minimized.

A point of concern is that the accelerometer biases b_y and b_z are not perfectly estimated by POD. Thus, $\Delta\boldsymbol{a}_y$ and $\Delta\boldsymbol{a}_z$ will contain residual biases, which are characterized as an offset plus a slow, non-linear drift. Since ignoring their presence would degrade our results, we suppress the residual biases by removing the average per orbit from the time series $\Delta\boldsymbol{a}_y$ and $\Delta\boldsymbol{a}_z$. This form of high-pass filtering retains only variations at suborbital frequency in the residual accelerations, such as those caused by dayside-nightside differences in radiation pressure, enabling us to estimate corrections to the radiation pressure model and the accelerometer scale factors.

Now that the objective function has been defined, we select the parameters to be co-estimated during the optimization. Similar to Hładczuk et al. (2024), we optimize the reflection and absorption coefficients for radiation for several materials: Teflon, Kapton, and the solar panel material. These coefficients are optimized under the constraints

$$0 \leqslant c_a \leqslant 1 \tag{14a}$$

$$0 \leqslant c_d \leqslant 1 \tag{14b}$$

$$0 \leqslant c_s \leqslant 1 \tag{14c}$$

$$c_a + c_d + c_s = 1, \tag{14d}$$

which considers the fact that the coefficients refer to the percentage of radiation being absorbed, as well as specularly and diffusely reflected. In Section 4, we only tune coefficients for visible light. This is motivated by the fact that the Earth's infrared is considered fairly constant, making it difficult to distinguish between effects from the radiation pressure and the accelerometer bias. However, as we saw at the end of the optimization, a geographical residual acceleration correlated with the Earth's infrared emission map, we will in Section 5 also tune the infrared coefficients of the nadir panel. This panel, due to its size and orientation, is a major contributor to radiation pressure acceleration resulting from the Earth's infrared emission.

In addition to the reflection and absorption coefficients, we also optimize the thermal model. For the thermal model, only the heat capacity of the solar arrays and the nadir panel will be optimized, as they are the primary contributors in the y- and z-directions. The conductivity, efficiency, and emissivity coefficients, as well as the heat capacity of the other panels, are not changed with respect to the initial values, provided in Section 3 and largely based on Siemes et al. (2023). For GRACE-FO, the thermal model could be tuned separately using measurements from thermistors located on the outside of the solar arrays (Hładczuk et al., 2024). However, for GRACE, thermistors are located beneath the insulation under the solar arrays. As a consequence, their measurements do not reflect the outside temperature of the solar arrays. Further, the number of insulating layers is unclear, rendering the thermistor measurements unusable for our purposes. Therefore, the thermal model will be optimized in conjunction with the reflection and absorption coefficients, rather than estimating them separately.

Finally, the accelerometer scale factors S_y and S_z are also optimized. Several optimization strategies will be outlined, where no scale factors, only the y-axis scale factor, or both the y- and z-axis scale factors are optimized, along with the thermal and radiation pressure models. The accelerometer bias is typically considered a slowly varying quantity and, because the signal is high-pass filtered, is not expected to have a significant influence. However, after optimizing the radiation pressure model, a clear feature remains in the residual acceleration in the geographical domain, correlated with the magnetic field that the satellite experiences. To mitigate this issue, a cross-track bias that depends on the magnetic field vector components will be introduced in Section 5.

3. Data and models

With the objective function and optimization parameters in place, we need to decide which data to use for the optimization. Since GRACE-A and GRACE-B are in similar orbits and have only a difference of 180° in yaw, we expect them to observe the same environment. Therefore, we can tune the radiation pressure model using data from one satellite and use the other satellite to verify that the model has been properly tuned and is not merely absorbing accelerometer noise or other errors. Therefore, the optimization will be performed using GRACE-A measurements only, but the obtained results will be assessed for both satellites. If the optimization is indeed performing as expected, a similar improvement in model quality should be observed in GRACE-A and GRACE-B, thereby verifying the method's validity.

Table 1 lists the data and models used in this work. Table 2 highlights the utilized GRACE data products. The thermal model parameters and the absorption and reflection coefficients are replicated in Tables 3 and 4 for convenience and are primarily based on Siemes et al. (2023). In these tables, the values shown in bold are optimized within this work. The ones underlined are only optimized during the extended optimization discussed in Section 5.

A special note is needed regarding the heat capacity of the solar panels. Contrary to previous work, we assume that the solar panels have a fixed heat capacity per unit area. Therefore, we can optimize the heat capacity of the zenith panel and scale it accordingly to obtain the heat capacity of the side panels. We also introduce the efficiency of solar panels, which is the fraction of absorbed radiation converted into electricity (Hładczuk et al., 2024). The efficiency is the fraction of the panel covered by solar cells (88% for the side solar panels and 83% for the zenith solar panel, estimated from images), multiplied by the efficiency of the individual solar cells ($\approx 18\%$), resulting in the values shown in the last column of Table 3.

Finally, similar to Hładczuk et al. (2024), we use separate reflection and absorption coefficients for the Kapton present on the apron and the antenna, and the Kapton covering the front and rear panels. This choice is motivated by the Kapton on the apron being slightly wrinkled, whereas it is flat on the front and rear, leading to slightly different reflections.

To minimize the impact of aerodynamic modeling errors, including those stemming from the thermosphere model used in the calculation of $\boldsymbol{C}_{\text{aero}}$, we use GRACE data from 2009. Then, solar activity was close to its minimum within the 11-year solar cycle, and the GRACE satellites' altitude was still relatively high at approximately 470 km. Both effects together result in low atmospheric drag and, thus, a small aerodynamic acceleration compared to radiation pressure acceleration, especially in the cross-track and radial direction. This ratio is illustrated in Fig. 1, which displays the contributions in the three main directions. In the along-track direction (x), the aerodynamic acceleration still contributes significantly. However, in the cross-track (y) and radial (z) directions, this is not the case, and the variation is mainly determined by radiation pressure. In the cross-track direction, temporal variation is mainly driven

Table 1
References for used models and data.

Radiation pressure modeling	
Initial radiation pressure model	Siemes et al. (2023), see also Tables 3 and 4
Thermal inertia model type	Wöske et al. (2019); Hładczuk et al. (2024)
Earth's albedo and infrared emission	Doelling et al. (2016) (CERES SYN1deg Hourly 4.2)
Solar irradiance at 1 au	Loeb et al. (2009) (CERES EBAF2.8)
Shadow function (Earth blocking Sun)	Robertson et al. (2015)
Shadow function (Moon blocking Sun)	Montenbruck and Gill (2000)
Aerodynamic modeling	
Force coefficients	March et al. (2019)
Horizontal wind	Drob et al. (2015) (HWM 14)
Atmospheric temperature and composition	Emmert et al. (2022) (NRLMSIS 2.1)
GRACE data	
GRACE Level 1B data	GeoForschungsZentrum (GFZ) Information System and Data Center (ISDC) on https://isdc.gfz.de
Initial calibration coefficients	Method of Siemes et al. (2023) with updated models

Table 2
GRACE products used within this work.

ACC1B	Accelerometer measurements
GNV1B	Position and velocity in ECEF
MAG1B	Magnetometer measurements
MAS1B	Mass
SCA1B (v3)	Attitude
THR1B	Thruster firing information

by solar and thermal radiation pressure. In the radial direction, the same holds, but Earth's radiation pressure also plays a role. It can be observed that the infrared Earth radiation pressure has contributions in the range -9 nm s^{-2} $\pm$ 4 nm s^{-2}, while the visible contribution shows values of -7.5 nm s^{-2} $\pm$ 7.5 nm s^{-2}. This confirms that the variation caused by the visible contribution is indeed higher than that caused by the infrared.

Table 3
GRACE initial thermal radiation panel model based on Siemes et al. (2023). Internal heat generation $P_{\text{gen}} = 70\,\text{W}$, heat capacity $C_{\text{body}} = 100\,\text{kJ} \cdot \text{K}^{-1}$. The values shown in bold will be optimized in the remainder of this work. The criteria for selecting which parameters to optimize are discussed in Section 2.2.

Panel	Material	A_j [m^2]	$n_{x,j}$ [–]	$n_{y,j}$ [–]	$n_{z,j}$ [–]	C_j [J K^{-1}]	k_j [W K^{-1}]	e_j [–]
Zenith	Solar array	2.1673620	0.0	0.0	−1.0	**5000**	0.10	0.15
Nadir	Teflon	6.0711120	0.0	0.0	1.0	**10000**	0.50	
Port (outer)	Solar array	3.1554792	0.0	−0.766044	−0.642787	**7280**	0.15	0.16
Port (inner)	Kapton (A/A)	0.2282913	0.0	0.766044	0.642787	500	0.10	
Starboard (outer)	Solar array	3.1554792	0.0	0.766044	−0.642787	**7280**	0.15	0.16
Starboard (inner)	Kapton (A/A)	0.2282913	0.0	−0.766044	0.642787	500	0.10	
Front (panel)	Kapton (F/R)	0.9551567	−1.0	0.0	0.0	1000	0.10	
Rear (panel)	Kapton (F/R)	0.9551567	1.0	0.0	0.0	1000	0.10	
Front (antenna)	Kapton (A/A)	0.0461901	0.0	0.0	1.0	400	0.01	
Rear (antenna)	Kapton (A/A)	0.0461901	0.0	0.0	−1.0	400	0.01	
Port (antenna)	Kapton (A/A)	0.0461901	0.0	−1.0	0.0	400	0.01	
Starboard (antenna)	Kapton (A/A)	0.0461901	0.0	1.0	0.0	400	0.01	

Table 4
Absorption and reflection coefficients for GRACE materials based on Siemes et al. (2023). The values shown in bold will be optimized in the remainder of this work; the underlined values have only been optimized in Section 5. The criteria for selecting which parameters to optimize are discussed in Section 2.2.

Material	$c_{d,\text{vis}}$ [–]	$c_{s,\text{vis}}$ [–]	$c_{a,\text{vis}}$ [–]	$c_{d,\text{ir}}$ [–]	$c_{s,\text{ir}}$ [–]	$c_{a,\text{ir}}$ [–]
Kapton (Apron/Antenna)	**0.26**	**0.40**	**0.34**	0.15	0.23	0.62
Kapton (Front/Rear)	**0.26**	**0.40**	**0.34**	0.15	0.23	0.62
Solar arrays	**0.05**	**0.23**	**0.72**	0.16	0.03	0.81
Teflon	**0.06**	**0.82**	**0.12**	**0.06**	**0.19**	**0.75**

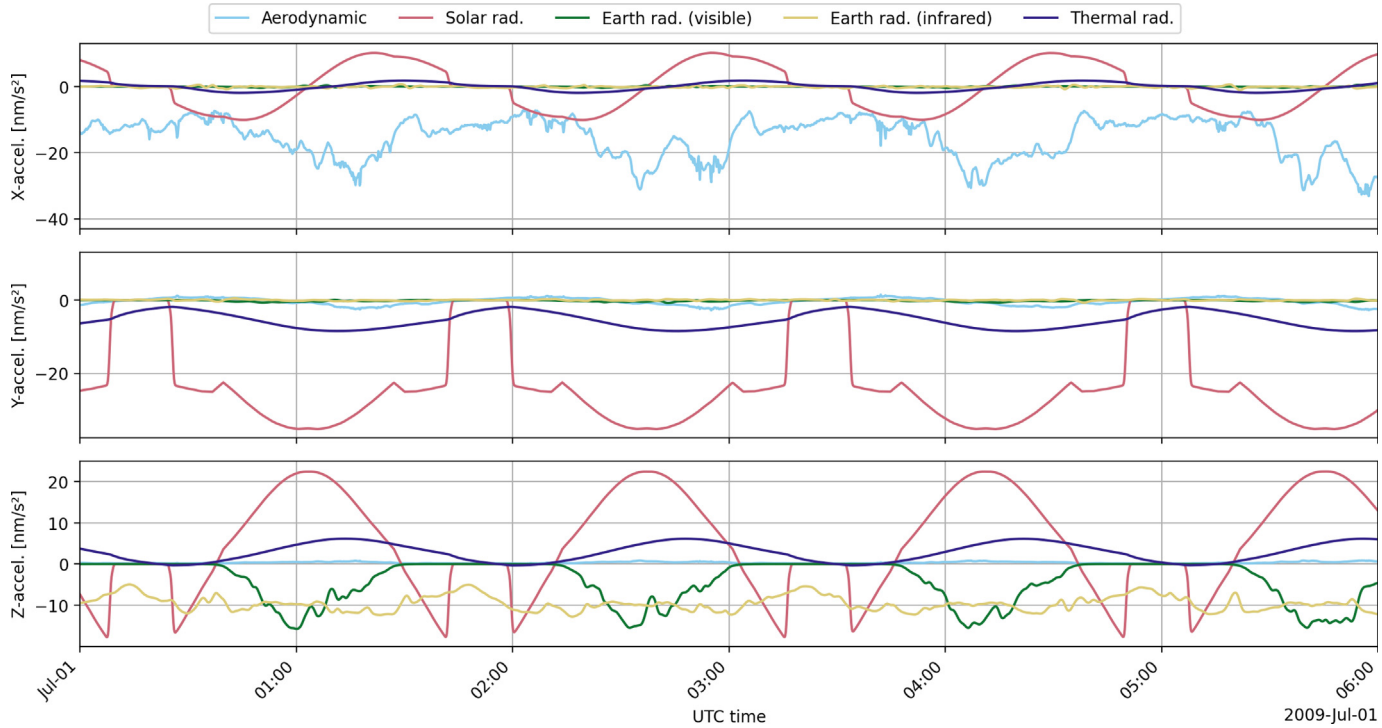

Fig. 1. Contribution of aerodynamic, solar radiation pressure, Earth's radiation pressure (visible and infrared), and thermal radiation pressure acceleration in the three SRF directions for GRACE-A.

Because radiation pressure modeling depends on solar radiation, the shadow function will be important for analyzing the results. Fig. 2 shows the shadow function for GRACE-A in 2009 as a function of the argument of latitude and time. Due to the similar orbits of GRACE-A and GRACE-B, the shadow function is nearly the same for GRACE-A and GRACE-B.

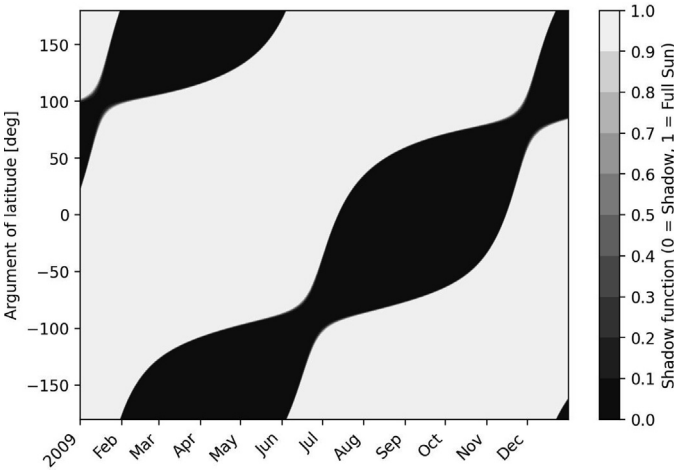

Fig. 2. Shadow function as perceived by GRACE-A in 2009. White indicates that the satellite is in full sunlight, while black indicates that it is in the Earth's shadow. Note that we use the Robertson et al. (2015) shadow function to model the eclipse, resulting in smooth transitions from full sunlight to Earth's shadow. and vice versa.

4. Joint optimization of radiation pressure model and accelerometer scale factors

Fig. 3 shows the y- and z-residuals between the modeled and measured accelerations as a function of time and argument of latitude, based on the POD-derived scale factors and using the initial model as defined in Section 3. Remember that we apply high-pass filtering by removing the mean per orbit, so only variations shorter than one orbit are shown in this visualization. The argument of the latitude axis is obtained by interpolating the residuals onto predefined argument of latitude values with a resolution matching the average resolution of the original argument of latitude. Furthermore, 1 year of data corresponds to about $16 \times 365 = 5840$ orbital revolutions, so we would need that many pixels in the temporal direction to fully display the data. Since such a high resolution is unreasonable, we calculate the daily average residual per argument of latitude to reduce the figure's required resolution. Note that we calculate the daily average residuals in a subsequent step after the high-pass filtering. White spots indicate where invalid data has been removed, e.g., because it was classified as an outlier. Another remark regards the colors, which are reversed for GRACE-A and GRACE-B when showing the y-residuals. Since the satellites orbit with their x-axes pointing toward each other and their z-axes pointing toward Earth, their y-axes point in approximately the opposite directions. Thus, commonalities in the y-residual due to the external environment are expected to have the

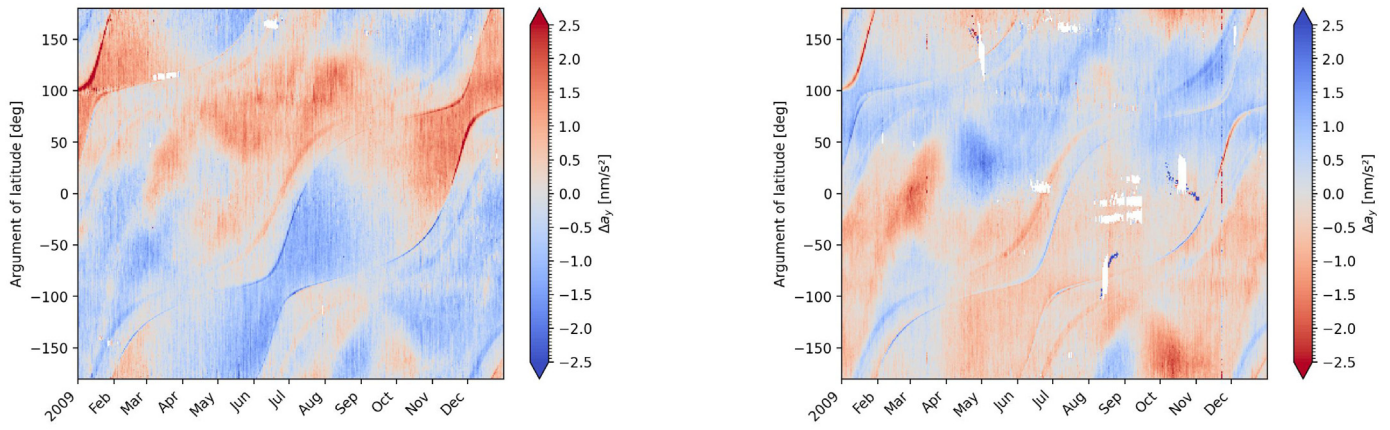

(a) GRACE-A Δa_y (b) GRACE-B Δa_y

Fig. 3. Residual accelerations in the y-direction for GRACE-A (left) and GRACE-B (right) with POD-derived scale factors using the initial radiation pressure model.

opposite sign in the satellite reference frame, and reversing the colors makes them easier to spot.

When comparing the obtained residuals to the shadow function shown in Fig. 2, a clear similarity can be seen. The large deviations occur along thin lines following the eclipse entry and exit points and, thus, might stem from inaccuracies in the shadow function. Further, a significant difference exists between the y-residuals of GRACE-A and GRACE-B, as evidenced by multiple locations showing opposite colors, e.g., in the shadow regions. Errors in the radiation pressure model cannot explain the difference, because the model is almost symmetric about the x-z plane, and such errors would yield the same color for GRACE-A and GRACE-B, thanks to the reversed color scale for GRACE-B. This fact suggests that accelerometer data calibration is a likely culprit for the difference. Since bias effects are removed by high-pass filtering, only the scale factors remain as a possible cause, motivating us to estimate them in conjunction with the radiation pressure model.

In this work, we will assess whether estimating the scale factors for the y- and z-axes during surface property optimization results in significantly smaller residual accelerations. The following cases are investigated:

- **POD y- and z-axis scale factors (PY-PZ)**: We tune the radiation pressure model without changing the scale factors.
- **Tuned y-axis scale factor and POD z-axis scale factor (TY-PZ)**: We tune the radiation pressure model together with the y-axis scale factor, leaving the z-axis scale factor unchanged.
- **Tuned y- and z-axis scale factors (TY-TZ)**: We tune the radiation pressure model together with y- and z-axis scale factors.

The abbreviation in brackets will be used in the remainder of this work to identify the cases.

One aspect that requires clarification before investigating the results is the definition of the various scale factors employed in this work. Three ways to obtain accelerometer scale factors are listed in Table 5. First of all, the *POD scale factor* refers to the value derived using POD, i.e., before any optimization. The other two types of scale factors, labeled *a priori* and *a posteriori*, result from an optimization. The a priori scale factor denotes the value obtained during the radiation pressure model tuning phase, in which the model and scale factor are jointly optimized using data from a single selected satellite (GRACE-A in this work). The a priori scale factor is instrument-specific and therefore valid only for one satellite, while the radiation pressure model is valid for both satellites. To avoid tuning the full radiation pressure model every time we want to obtain a scale factor, we can also tune the scale factors using a previously tuned radiation pressure model. This is especially useful in our case, where we tune the radiation pressure model for GRACE-A and reuse it for GRACE-B. The scale factors obtained by this shortcut are the a posteriori scale factors. The a priori and a posteriori scale factors should be nearly identical if they are both estimated, as is the case for GRACE-A. To compare the accelerometer measurements with the modeled accelerations in a fair way, we will always apply a posteriori scale factors for both the y- and z-axes. Also, the final proposed scale factors will stem from the a posteriori scale factors. The POD-derived calibration is independent of the radiation pressure model

Table 5
Definition of different scale factors used within this work.

POD scale factor	Scale factor derived from precise orbit determination.
A priori scale factor	Scale factor tuned along with the radiation pressure model.
A posteriori scale factor	Scale factor tuned using a fixed radiation pressure model.

but depends on the selected scale factor. However, as we update both the scale factor and bias in the cross-track and radial directions, there is no need for a feedback mechanism between the orbit determination and the results we obtain.

In the following, we discuss our results based on different criteria. First, the tuned surface absorption and reflection coefficients as well as the thermal model properties are discussed in Section 4.1. Afterwards, Section 4.2 discusses the obtained scale factors and compares them with other results from the literature. Section 4.3 discusses the obtained reduction in acceleration residual and investigates the agreement between GRACE-A and GRACE-B residuals. The latter will reveal significant, yet unmodeled effects in the residuals.

4.1. Obtained radiation pressure model

Table 6 shows the surface and thermal model properties for the initial model as well as the tuned radiation pressure model for the different optimization strategies. For the Kapton foil covering the apron and the antenna, we observe a very specular surface (coefficient c_s is close to 1) in all optimized cases, which is relatively far from the initial values reported by Siemes et al. (2023). The TY-TZ has the lowest specular coefficient of the three optimized cases. Note that the effect of this material on the acceleration is limited due to its small area and is therefore also harder to properly optimize. The other materials make a significantly greater contribution. For the Kapton on the front and rear panels of the satellites, the TY-PZ case has reached one of the constraint lines, as evidenced by $c_d = 0$. The other two optimizations give, especially for the diffuse reflection, very similar values to the initial radiation pressure model. A diffuse reflection on the front and rear panel can be clearly seen in pre-launch images, and there is no reason to believe that the surface would become much more specular in orbit.

When examining the solar array coefficients, we observe that the optimized absorption coefficients (c_a) are all larger than the initial value. The increase in absorption coefficient relative to the initial value is 10% for the PY-PZ optimization strategy, 8% for the TY-PZ approach, and 4% for the TY-TZ approach. The surface absorption may indeed increase over time due to roughening or contamination, e.g., due to thruster firings or the adsorption of atomic oxygen. However, since there is no reason to believe that the absorption of solar panels has increased significantly in orbit, the TY-TZ optimization likely provided the most accurate result. Another observation is that the thermal capacity of the optimized cases is significantly higher than in the initial case, but this is not considered a limiting factor, as it was only roughly estimated previously.

Finally, for the Teflon panel, we see that in the TY-TZ case, the diffuse reflection is almost completely removed, and all light is absorbed or specularly reflected. In this case, the coefficients of the other two are closer to the initial values. On the other hand, the heat capacity of the TY-TZ optimization strategy is closest to the initial model. However, given the rough estimate used in the initial radiation pressure model, this should not be considered a key decision factor. It is important to note that the acceleration of the Teflon panel is also partly driven by the infrared radiation emitted by the Earth. Therefore, the coefficients may shift to more extreme values to partially compensate for errors in the infrared radiation coefficients.

Table 6
Comparison of reflection and absorption coefficients for visible light and thermal capacities per material and optimization case. The thermal capacity is given per unit area.

Material	Strategy	c_d [–]	c_s [–]	c_a [–]	C_j [J K^{-1} m^{-2}]
Kapton apron/antenna	Initial	0.26	0.40	0.34	
	PY-PZ	0.00	0.95	0.05	
	TY-PZ	0.00	1.00	0.00	
	TY-TZ	0.00	0.86	0.14	
Kapton front/rear	Initial	0.26	0.40	0.34	
	PY-PZ	0.22	0.11	0.67	
	TY-PZ	0.00	0.15	0.85	
	TY-TZ	0.26	0.18	0.56	
Solar arrays	Initial	0.05	0.23	0.72	2307
	PY-PZ	0.01	0.20	0.79	2390
	TY-PZ	0.02	0.20	0.78	2493
	TY-TZ	0.02	0.23	0.75	3380
Teflon	Initial	0.06	0.82	0.12	1647
	PY-PZ	0.06	0.85	0.09	881
	TY-PZ	0.07	0.84	0.09	1270
	TY-TZ	0.00	0.86	0.14	1481

4.2. Accelerometer scale factors

A second factor to consider when evaluating the optimization cases is the scale factors obtained for the accelerometers. Table 7 shows the a priori and a posteriori scale factors for GRACE-A and GRACE-B. The comparison of the a priori and a posteriori scale factors reveals a maximum deviation of 0.1%, confirming our earlier claim that the two are almost identical. Furthermore, Table 7 shows scale factors provided in the literature. The scale factors determined by Teixeira Da Encarnação et al. (2020) have been estimated during the gravity field determination, while the others are POD-based scale factors. For the scale factors determined by Koch et al. (2018), a distinction is made between 'NGO' and 'NGM' approaches. The NGO approach relied on orbit determination to calibrate the acceleration (similar to POD), whereas the NGM approach used non-conservative forces for that purpose, similar to our a posteriori scaling. The results from the NGO and NGM approaches differ significantly, indicating that large differences in scale factors derived from POD and non-gravitational force models can be expected. Furthermore, their scale factors differ significantly from those of the others. This could be attributed to the short time span

Table 7
GRACE accelerometer scale factors from different optimization strategies and institutes for 2009, except for Koch et al. (2018) who base their results on data from June to August 2008. For the optimized scale factors presented in this work, the a priori (if present) and a posteriori scale factors are shown. The scale factors are in the scientific reference frame (SRF) and are shown to three digits. Blank values indicate that these values are not estimated and the POD-derived values are used (for our a priori and a posteriori values) or are not present (for the literature values).

		GRACE-A			GRACE-B		
		S_x [–]	S_y [–]	S_z [–]	S_x [–]	S_y [–]	S_z [–]
TU Delft	POD	0.960	0.965	0.953	0.945	0.920	0.948
TY-PZ	A priori		0.950				
TY-TZ	A priori		0.927	0.896			
Initial	A posteriori		0.944	0.935		0.958	0.931
PY-PZ	A posteriori		0.954	0.947		0.969	0.945
TY-PZ	A posteriori		0.950	0.944		0.964	0.943
TY-TZ	A posteriori		0.928	0.896		0.942	0.894
Bettadpur (2009)		0.960	0.980	0.949	0.947	0.984	0.930
Helleputte et al. (2009)		0.960			0.950	1.050	1.000
Bezděk (2010)		0.961	0.980	0.940	0.947	0.970	0.920
Koch et al. (2018) (NGO)					1.310	1.260	0.180
Koch et al. (2018) (NGM)					0.920	0.740	1.090
Vielberg et al. (2018)		0.939	0.922	0.941	0.931	0.916	0.938
Teixeira Da Encarnação et al. (2020)		0.956	0.794	0.959	0.942	0.778	0.954
Siemes et al. (2023)		0.940	0.960	0.930	0.950	0.970	0.950
Wöske et al. (2024)		0.959	0.952	0.952	0.944	0.958	0.953

(3 months) of data used for scale factor tuning and the low acceleration signal during those periods.

We observe that our initial, PY-PZ, and TY-PZ values fall within the same range as the POD-derived scale factors from other authors, whereas the TY-TZ case yields scale factors that are a few percent lower for both the y- and z-axis.

4.3. Residual accelerations

The final point is assessing the optimization cases based on the residual acceleration. Table 8 shows the root-mean-square (RMS) of the high-pass filtered residual acceleration. The RMS of the high-pass filtered accelerometer measurement is also shown for reference. Note that if the accelerometer is scaled, the signal's RMS is scaled accordingly. Here, we see that the RMS of the signal is about 14 nm s^{-2} for the y-direction and 15 nm s^{-2} for the z-direction, which is more than ten times larger than the RMS of the residual.

The second and third row of Table 8 show the RMS of the residual acceleration using the initial radiation pressure model with POD and a posteriori scale factors, respectively. A significant residual decrease is already present when only a posteriori scale factors are included. By moving from the initial case to the PY-PZ case, then further to the TY-PZ case, and finally to the TY-TZ case, the RMS of the residuals is reduced each time, which is not surprising because we estimate more parameters from one case to the next. The overall reduction in RMS is larger for the z- than for the y-residual, which could be explained by the fact that the initial case was optimized based on the latter while ignoring the former (Siemes et al., 2023). The RMS for the PY-PZ and TY-PZ cases is very similar, meaning that estimating only the y-axis scale factor does not significantly improve the results. However, when also

Table 8
RMS of the acceleration residual based on the posteriori scale factors. The first two rows give the RMS of the total unscaled acceleration and the RMS of the initial model with POD scale factors.

	GRACE-A		GRACE-B	
	RMS(Δa_y) [nm s^{-2}]	RMS(Δa_z) [nm s^{-2}]	RMS(Δa_y) [nm s^{-2}]	RMS(Δa_z) [nm s^{-2}]
Signal	13.917	15.400	13.856	15.053
Initial (POD)	0.899	0.951	1.138	1.002
Initial	0.847	0.907	1.011	0.968
PY-PZ	0.837	0.679	0.982	0.726
TY-PZ	0.824	0.679	0.966	0.729
TY-TZ	0.787	0.644	0.932	0.674

estimating the z-axis scale factor, we observe another significant reduction in the RMS for both y- and z-residuals.

Since the radiation pressure model was optimized using only GRACE-A data, the decrease in the RMS for GRACE-B indicates an improvement in model accuracy. The RMS of the y-residuals is larger for GRACE-B than for GRACE-A, while this is less the case for the z-residuals. However, the RMS reduction from the initial case to the TY-TZ case for the y-residuals is 7% for GRACE-A and 8% for GRACE-B, i.e., increasing the accuracy for both satellites. For the z-residuals, the RMS reduction is even larger with 29% and 30% for GRACE-A and GRACE-B, respectively.

Figs. 4, 5 show the residual in the y- and z-directions for GRACE-A and GRACE-B for the initial and the TY-TZ case. We observe a reduction in the residual of the TY-TZ case, particularly in the z-direction, compared to the initial case. When comparing Fig. 4 to Fig. 3, it can be observed that including a posteriori scale factors already reduces the deviation for the initial case in the y-direction significantly. However, the residual decrease from the initial radiation pressure model to the TY-TZ radiation pressure model does only slightly change the obtained residuals in this direction. In the z-direction, however, the residual reduction is more pronounced. High deviations, e.g., at the encircled locations, come at the cost of a slight increase in the residuals at other locations, but overall the residuals are reduced. Note that even though the optimization of the radiation pressure model is only performed using GRACE-A data, the GRACE-B residuals are also decreasing. Appendix A shows the same visualization for all optimization cases for the interested reader. There, moving from the initial case to the PY-PZ case reduced the z-residual primarily, while also reducing some of the residuals in the y-residual. The difference between the PY-PZ and TY-PZ cases is very small, as the RMS values in Table 8 already suggested. The difference between the TY-PZ and TY-TZ cases is larger, where the latter clearly leads to the smallest residuals.

Another way to analyze the GRACE-A and GRACE-B residuals is to check for common errors. Since the satellites were in practically the same orbit, one following the other with a time delay of only about 29 s, we would expect them to experience very similar accelerations when correcting for

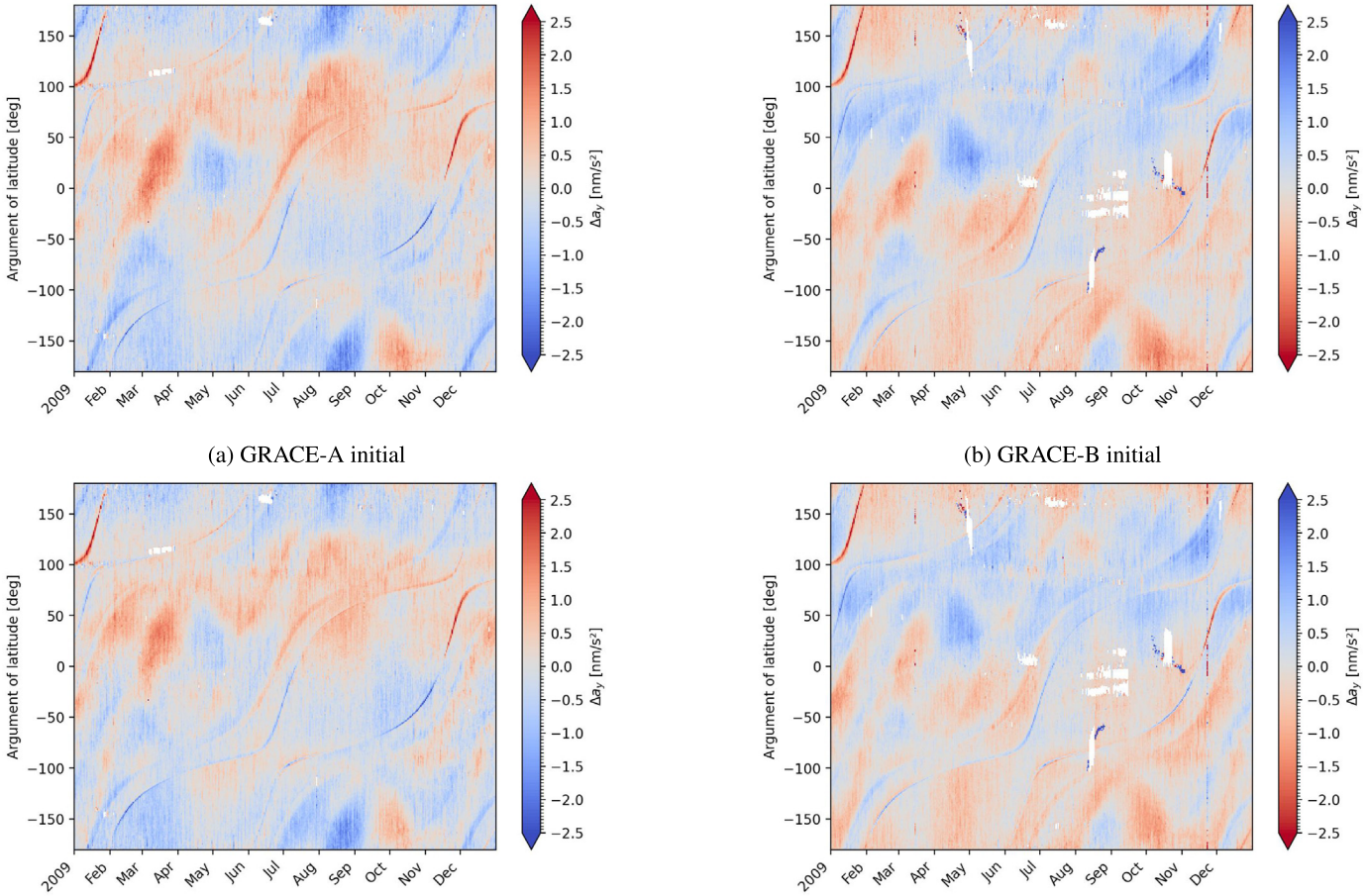

(a) GRACE-A initial

(b) GRACE-B initial

(c) GRACE-A TY-TZ

(d) GRACE-B TY-TZ

Fig. 4. Residual accelerations in the y-direction for GRACE-A (left) and GRACE-B (right) with a posteriori estimated scales using the initial (top) and TY-TZ (bottom) radiation pressure model.

that time offset. As explained before, we expect that any common errors, particularly those from the radiation pressure model, will appear almost identical in the z-residual and have the opposite sign in the y-residual due to the satellites' relative attitudes. Thus, the common errors should cancel in the sum of the y-residual and difference of the z-residual of GRACE-A and GRACE-B, which we show in Fig. 6.

For the z-residual (Fig. 6b), the difference is much smaller than the residual in Fig. 5. This observation means that the z-residual is dominated by radiation pressure modeling errors, while the other remaining errors are much smaller. For the y-residual (Fig. 6a), most variations over time are removed in the difference. However, there is an unexpected offset in the Northern Hemisphere (between 0° and 180° argument of latitude).

To further analyze the issue, we calculated the median residual in 2009 for 5° by 5° geographic grid cells for both satellites, shown in Fig. 7. Note that the median was calculated for the entire year, using both descending and ascending tracks. For the y-residual, we observe a clear pattern with the same sign (opposite colors) for both satellites. This observation means that the pattern points in opposite directions when shown in a common reference frame, e.g., the orbit reference frame. The pattern of the y-residual closely resembles the magnetic field measured by the onboard magnetometers, as shown for the interested reader in Appendix B. By trial and error, we found that it can be modeled as a sum of linear and quadratic terms of the x- and z-components of the magnetic vector. These findings suggest that the y-residuals are not caused by a physical acceleration (e.g., the Lorentz force) but might be attributed to an unmodeled instrument effect.

A similar dependency on the magnetic field for the roll angular acceleration bias has been observed by Harvey and Sakumura (2019). The roll angular acceleration is formed using the same electrode pairs as the cross-track acceleration. One possible explanation is that this is caused by the accelerometer instrument's dependency on the magnetic field. A theoretical study of the sensitivity of inertial accelerometers to slow-varying magnetic fields was conducted by Wang et al. (2025), indicating that these fields may indeed affect measurements in a quadratic fashion.

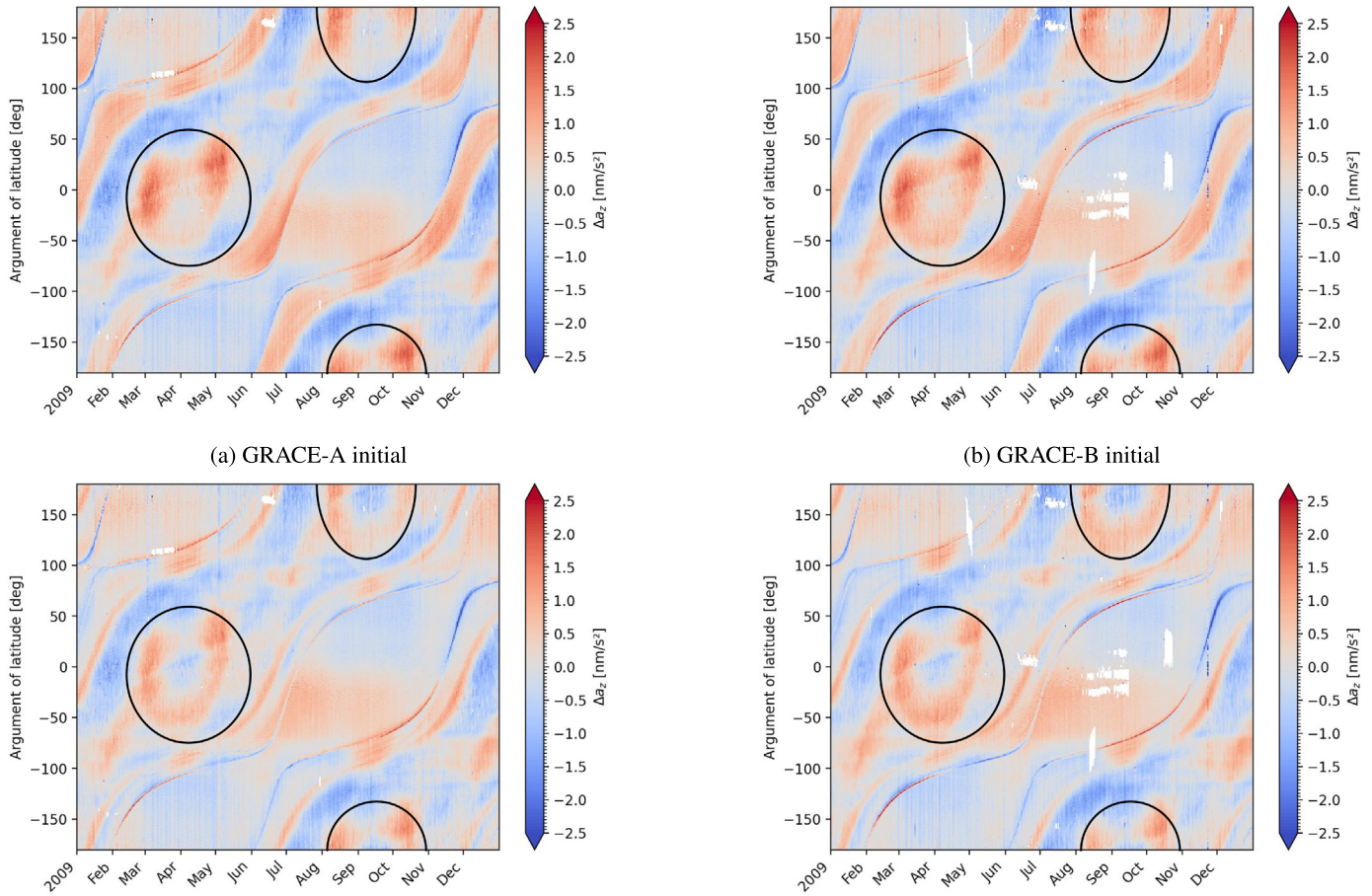

(a) GRACE-A initial

(b) GRACE-B initial

(c) GRACE-A TY-TZ

(d) GRACE-B TY-TZ

Fig. 5. Residual accelerations in the z-direction for GRACE-A (left) and GRACE-B (right) with a posteriori estimated scales using the initial (top) and TY-TZ (bottom) radiation pressure model.

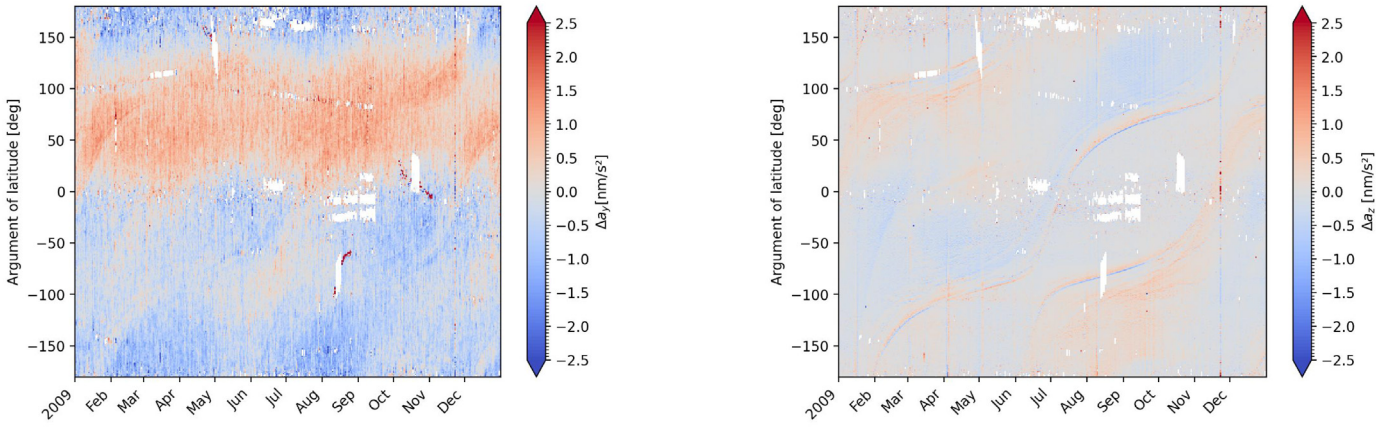

(a) Sum of y-residual

(b) Difference of z-residual

Fig. 6. Sum of the y-residual for GRACE-A and GRACE-B (left), difference of the z-residual for GRACE-A and GRACE-B (right) using a posteriori scale factors and the TY-TZ radiation pressure model.

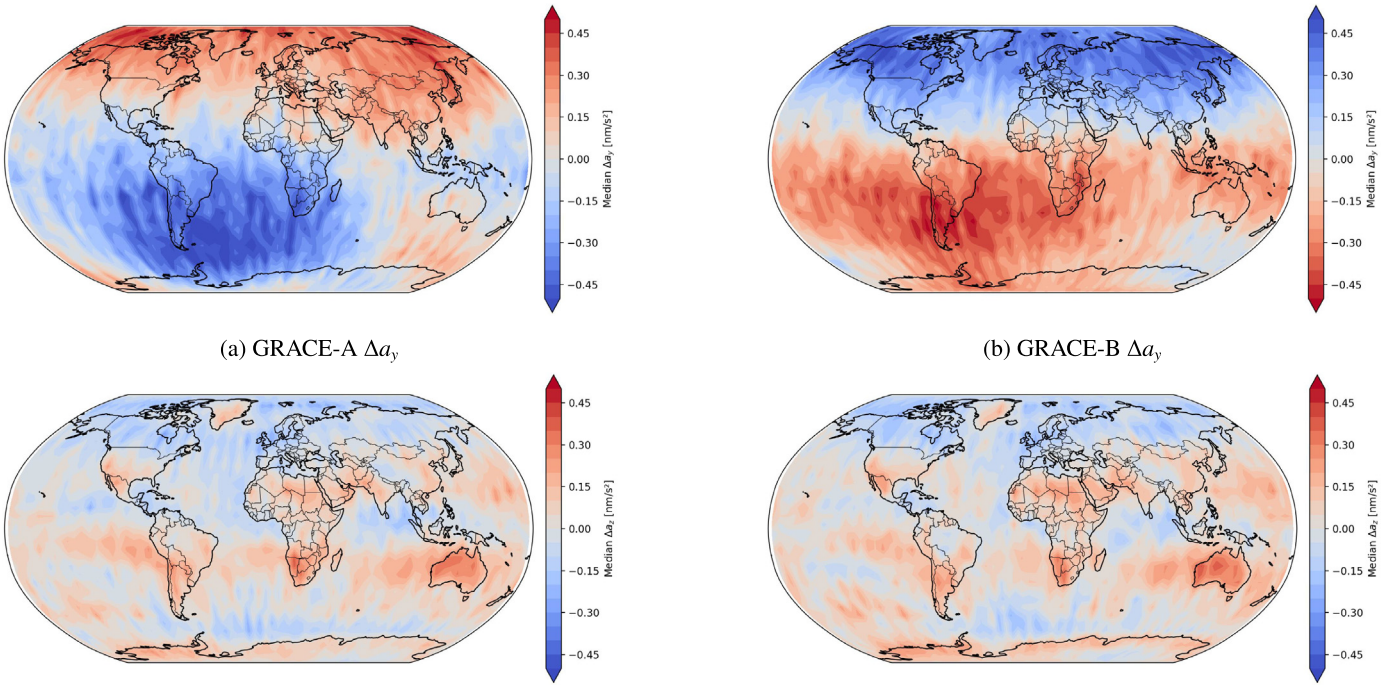

(a) GRACE-A Δa_y

(b) GRACE-B Δa_y

(c) GRACE-A Δa_z

(d) GRACE-B Δa_z

Fig. 7. Median residual per 5° by 5° geographical grid cell for GRACE-A (left) and GRACE-B (right) in the cross-track (top) and radial (bottom) direction using a posteriori scale factors and the TY-TZ radiation pressure model.

We observe the bias only in the y-acceleration measurements. Thus, it could be related to the accelerometer design, which features a larger electrode size and a smaller electrode gap in this direction (Touboul et al., 2012). As a result, a lower detection voltage is required to center the proof mass in the accelerometer, which reduces achievable resolution but may also increase sensitivity to external disturbances.

Finally, it should be noted that in GRACE-FO, the control loop electronics have been placed inside the accelerometer's thermal enclosure (Kornfeld et al., 2019) to improve thermal and electromagnetic shielding compared to GRACE. A preliminary analysis on GRACE-C in 2019 indicates that no quadratic correction term is required and that the Lorentz force could possibly explain the linear terms. This comparison suggests that the GRACE

accelerometer may be affected by the magnetic field due to the limited electromagnetic shielding of its electronics.

The z-residual for GRACE-A and GRACE-B is very similar. This commonality suggests that it is caused by inaccuracies of the radiation pressure model. The residuals show a clear correlation to Earth's radiation pressure maps, shown for a selected month in Appendix C, particularly Earth's infrared emission (right panel). Since Earth's infrared radiation is primarily incident on the nadir panel and since the absorption and reflection coefficients for that panel have not been tuned, it is likely that errors in those coefficients are responsible for the z-residual.

5. Empirical magnetic-field-induced accelerometer bias and Teflon infrared coefficients tuning

The previous section identified two effects in the acceleration residuals that are not yet optimized. The first appears to cause a variation in the y-residual, which correlates with the x- and z-components of the magnetic field vector. Second, the analysis of the z-residual revealed the need to include the nadir panel's absorption and reflection coefficients for infrared radiation in the optimization. Since the TY-TZ case was the best-performing, we select it as the baseline and will expand it to address the aforementioned shortcomings.

Since no physical cause for the magnetic-field dependency could be found, we will address the magnetic-field influence by including an empirical magnetic-field-induced bias in the accelerometer measurements. The investigation of the geographical maps indicated that the accelerometer measurements should be corrected using both linear and quadratic terms of the x- and z-components of the magnetic vector in the SRF. The magnetic-field-induced bias is applied before scaling the accelerometer and is defined as

$$b_{y,\mathrm{mag}} = \sum_{i=x,z} \alpha_i B_i + \beta_i B_i^2, \tag{15}$$

where B indicates the components of the Earth's magnetic vector as measured by the onboard magnetometer. In cases of gaps or flagged outliers in the measurements, we use the International Geomagnetic Reference Field (IGRF) model (Alken et al., 2021).

In the following, we will discuss the results for the magnetic-field-induced bias in Section 5.1 and the expanded radiation pressure model in Section 5.2. The estimated scale factors are examined in Section 5.3, and the acceleration residuals are scrutinized in Section 5.4. Section 5.5 discusses the final results and summarizes all tuned parameters.

5.1. Magnetic-field-induced accelerometer bias

In this section, we review the magnitude of the magnetic-field-induced bias to be applied to the accelerometer measurements. We can estimate the magnetic-field-induced bias together with the radiation pressure model or after applying the fully optimized model. Analogously to the scale factors, we use the labels a priori and *a posteriori* to distinguish these options. Note that the a posteriori magnetic-field-induced bias is estimated together with the a posteriori scale factor for the y-axis, as they both affect the y-residuals. For GRACE-A, Table 9 shows the a priori and a posteriori estimated values, whereas for GRACE-B, only the a posteriori estimated values are available.

First, we observe good agreement between the a priori and a posteriori magnetic-field-induced biases, indicating high consistency across the estimation options. Second, the values obtained for GRACE-A and GRACE-B show the same sign. For the z-contribution, the magnitudes are similar, whilst for the x-contribution, the correction for GRACE-B is smaller than that for GRACE-A. The magnetic-field-induced bias is thus likely instrument-specific.

To indicate the magnitude of the magnetic-field-induced bias, Fig. 8 shows the bias as applied to the accelerometer measurements, where we removed the mean per orbit in the same way as for the residuals. It can be seen that the magnetic-field-induced bias variations have an amplitude of up to approximately ± 0.5 nm s^{-2}, consistent with the magnitude of the residuals observed in Figs. 6, 7.

5.2. Extended radiation pressure model tuning

As indicated earlier, we extend the TY-TZ case to include the estimation of the nadir panel's absorption and reflection coefficients for infrared radiation. The estimated coefficients for the TY-TZ - extended case are shown in Table 10, together with the initial and the TY-TZ case from Section 4.

For the Kapton on the apron, the TY-TZ - extended case moves to a more diffuse reflection compared to the TY-TZ case, while the Kapton on the front and rear panel

Table 9
Coefficients of the magnetic-field-induced bias in Eq. (15).

		Linear		Quadratic	
		α_x [nm s$^{-2}\mu$T^{-1}]	α_z [nm s$^{-2}\mu$T^{-1}]	β_x [nm s$^{-2}\mu$T^{-2}]	β_z [nm s$^{-2}\mu$T^{-2}]
GRACE-A	A priori	1.08×10^{-2}	6.74×10^{-3}	6.98×10^{-4}	3.79×10^{-4}
	A posteriori	1.30×10^{-2}	7.03×10^{-3}	6.91×10^{-4}	3.78×10^{-4}
GRACE-B	A posteriori	2.09×10^{-3}	7.64×10^{-3}	2.74×10^{-4}	2.72×10^{-4}

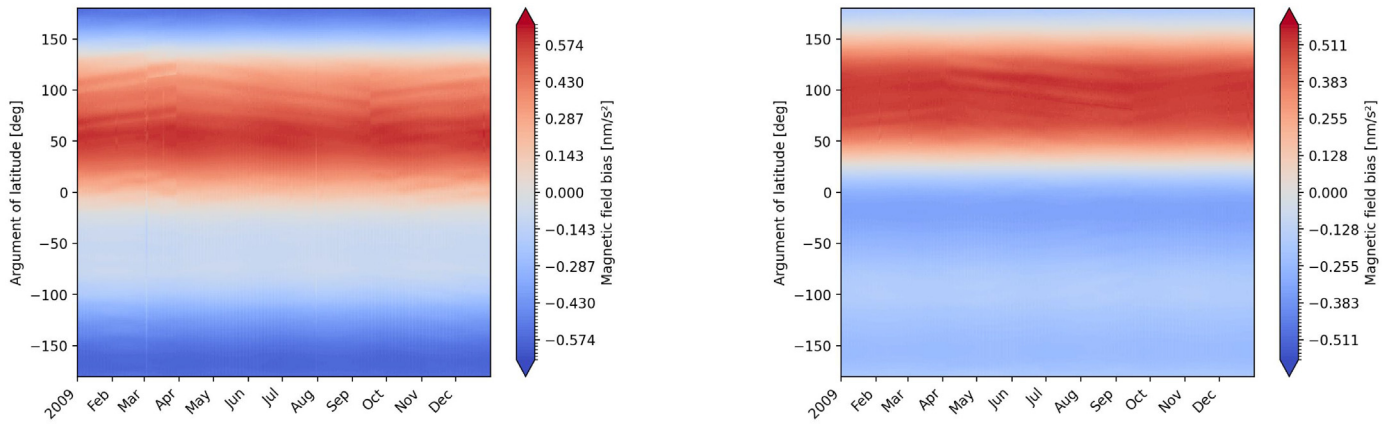

(a) GRACE-A (b) GRACE-B

Fig. 8. Magnetic-field-induced accelerometer bias for GRACE-A (left) and GRACE-B (right).

Table 10
Radiation pressure model parameters per optimization case. The thermal capacity is given per unit area.

Material	Strategy	c_d [–]	c_s [–]	c_a [–]	C_j [J K^{-1} m^{-2}]
Kapton apron/antenna	Initial	0.26	0.40	0.34	
	TY-TZ	0.00	0.86	0.14	
	TY-TZ - extended	0.08	0.88	0.04	
Kapton front/rear	Initial	0.26	0.40	0.34	
	TY-TZ	0.26	0.18	0.56	
	TY-TZ - extended	0.03	0.21	0.76	
Solar arrays	Initial	0.05	0.23	0.72	2307
	TY-TZ	0.02	0.23	0.75	3380
	TY-TZ - extended	0.03	0.24	0.73	3954
Teflon visible	Initial	0.06	0.82	0.12	1647
	TY-TZ	0.00	0.86	0.14	1481
	TY-TZ - extended	0.00	0.87	0.13	2732
Teflon infrared	Initial	0.06	0.19	0.75	
	TY-TZ				
	TY-TZ - extended	0.57	0.00	0.43	

is estimated to be less diffuse when comparing the same cases. The lower diffusivity is consistent with pre-launch images, where the Kapton on the front and rear panels is much more tightly applied than the Kapton on the apron, which will therefore wrinkle and become more diffuse. It is also worthwhile pointing out that the diffuse reflection coefficient for the Kapton on the apron reached the limit value of 0.00 for the TY-TZ case, which is not the case for the TY-TZ - extended case. Overall, the changes in the Kapton coefficients are the largest, which can be explained by their smaller contribution to the accelerations and, therefore, higher sensitivity to modeling errors such as the magnetic-field-induced bias.

For the solar arrays, the reflection and absorption coefficients obtained for the TY-TZ - extended case are closer to the values reported in the GRACE handbook than for the TY-TZ case. This observation is an important indicator of increased model accuracy, as a significant increase in the solar panel's absorption coefficient is not expected.

Finally, for the Teflon panel, the visible coefficients hardly change from the TY-TZ to the TY-TZ - extended case. However, the infrared absorption is reduced in the TY-TZ - extended case while the diffuse reflection is significantly increased. Furthermore, the thermal capacity of both the Teflon panel and the solar arrays is significantly higher in the TY-TZ - extended case than in the other cases. Note that the thermal capacity per unit area of the Teflon panel approaches that of the solar panels.

5.3. Accelerometer scale factors

The accelerometer scale factors of the TY-TZ - extended case (with magnetic-field-induced bias and nadir panel infrared tuning) are reported in Table 11 together with

Table 11
Scale factors of the TY-TZ - extended case compared to those of the TY-TZ case and the ones from POD.

		GRACE-A			GRACE-B		
		S_x [–]	S_y [–]	S_z [–]	S_x [–]	S_y [–]	S_z [–]
TU Delft	POD	0.960	0.965	0.953	0.945	0.920	0.948
TY-TZ	A posteriori		0.928	0.896		0.942	0.894
TY-TZ - extended	A priori		0.920	0.883			
TY-TZ - extended	A posteriori		0.916	0.879		0.915	0.878

those of the TY-TZ case and the POD scale factors. The a priori and a posteriori scale factors of the TY-TZ - extended case agree well for GRACE-A. Furthermore, the consistency between the GRACE-A and GRACE-B a posteriori scale factors is remarkably high. Comparing the TY-TZ - extended case with all other cases, we observe a further decrease in the scale factor. Note that the scale factors of both the TY-TZ and TY-TZ - extended cases are significantly lower than the values obtained from POD. It is likely that the other estimated parameters make the estimated scale factor less reliable. However, combining all estimated parameters, including the tuned scale factors, makes the total model more accurate and more consistent with accelerometer measurements, which was the primary goal of this work. Therefore, we accept the discrepancy between POD and non-gravitational model-derived scale factors.

5.4. Residual accelerations

As before, we inspect the residuals' RMS and their visualizations in the time-argument-of-latitude and geographic domains. Table 12 shows the RMS of the residuals for the TY-TZ and the TY-TZ - extended cases. Including the magnetic-field-induced correction reduces the RMS by 8% and 6% for GRACE-A and GRACE-B, respectively, which is an improvement of similar magnitude as for moving from the TY-PZ to the TY-TZ case (see Table 8). For the z-direction, the RMS reduces by approximately 5%.

Fig. 9 shows the obtained residuals of the TY-TZ - extended case as a function of time and argument of latitude. Similar patterns appear in the GRACE-A and GRACE-B y- and z-residuals, which was not the case for the y-residuals before. Furthermore, the residuals of the TY-TZ - extended case are indeed smaller compared to the other cases. The agreement between GRACE-A and GRACE-B is also confirmed in Fig. 10, in which the sum of the y-residuals and difference of the z-residuals between GRACE-A and GRACE-B is much smaller than the residuals. Thus, both y- and z-residuals are dominated by common effects, likely due to remaining inaccuracies in radiation pressure modeling. Finally, the geographical visualizations in Fig. 11 show that the y- or z-residuals are substantially smaller and less systematic than those in Fig. 7, although in the z-residual, a clear positive offset can be observed, e.g., over Greenland and Antarctica. Since the residual is defined as the modeled minus the measured acceleration (see Eq. (3)) and the z-direction points in the nadir direction, i.e., to Earth, a positive residual indicates that the acceleration due to either the albedo or the Earth's infrared emission at those locations is modeled systematically too low. Possible explanations include that the albedo and/or Earth's infrared emission maps underestimated albedo and/or Earth's infrared emission, or that we mismodeled the reflection type, noting that we currently assume a fully diffuse reflection for albedo, whereas it could be partially specular for the ice sheets. A method accounting for Earth's surface properties

Table 12
RMS of the acceleration residual with a posteriori scale factors included in both axes. The first row indicates the RMS of the accelerometer measurements before the scale factor is applied.

	GRACE-A		GRACE-B	
	RMS(Δa_y) [nm s^{-2}]	RMS(Δa_z) [nm s^{-2}]	RMS(Δa_y) [nm s^{-2}]	RMS(Δa_z) [nm s^{-2}]
Signal	13.917	15.400	13.856	15.053
Initial	0.847	0.907	1.011	0.968
TY-TZ	0.787	0.644	0.932	0.674
TY-TZ - extended	0.719	0.610	0.872	0.634

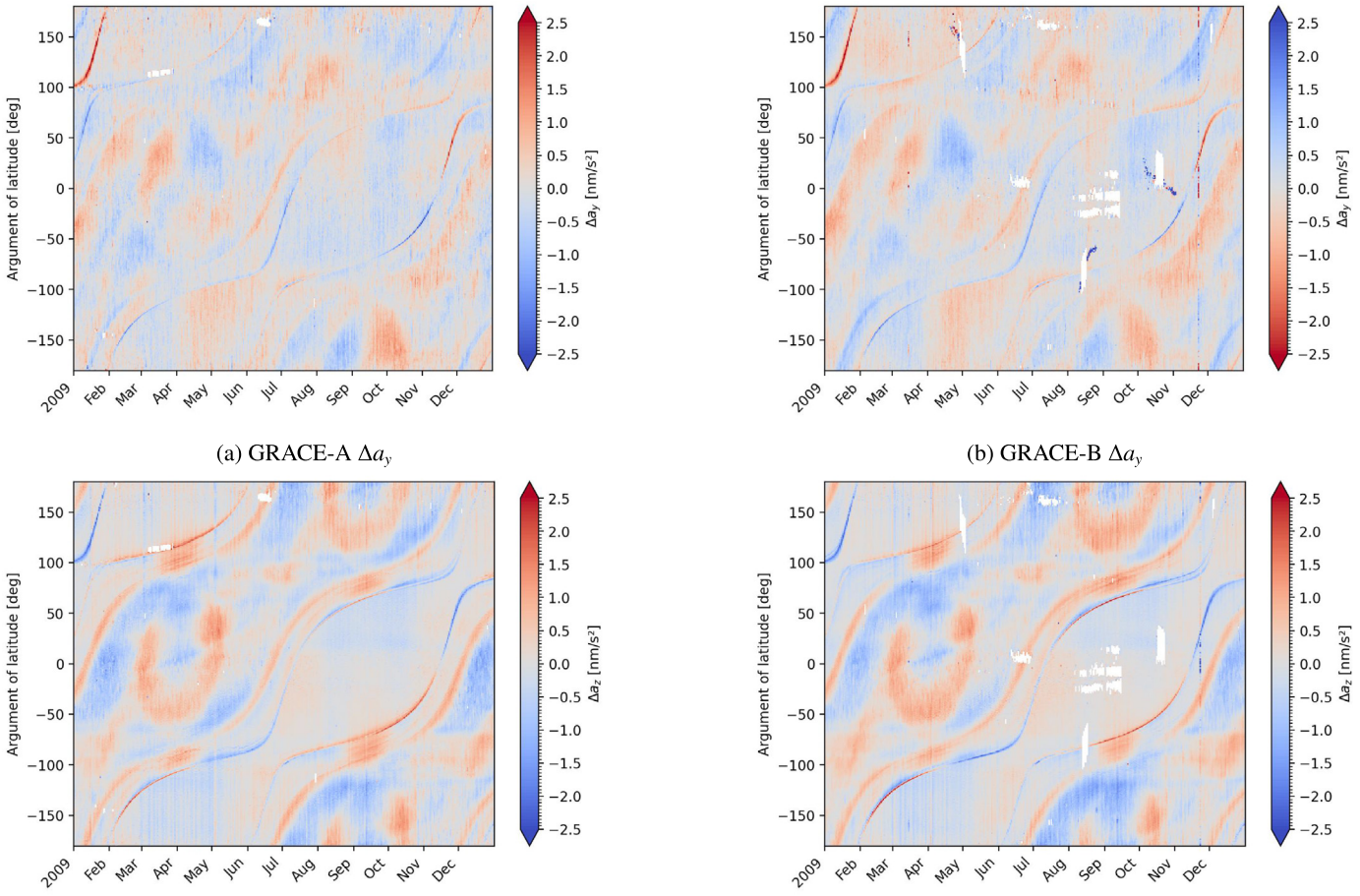

(a) GRACE-A Δa_y (b) GRACE-B Δa_y

(c) GRACE-A Δa_z (d) GRACE-B Δa_z

Fig. 9. Residual accelerations in the y- (top) and z-direction (bottom) for GRACE-A (left) and GRACE-B (right) with a posteriori estimated scales using the TY-TZ - extended radiation pressure model.

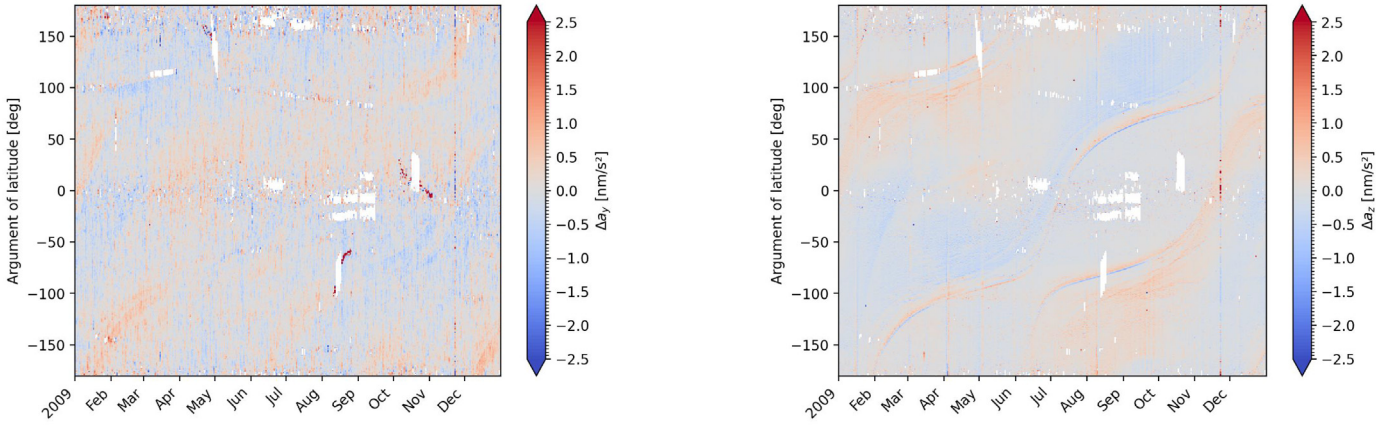

(a) Sum of y-residual (b) Difference of z-residual

Fig. 10. Sum of the y-residual for GRACE-A and GRACE-B (left) and difference of the z-residual for GRACE-A and GRACE-B (right) using a posteriori scale factors and the TY-TZ - extended radiation pressure model.

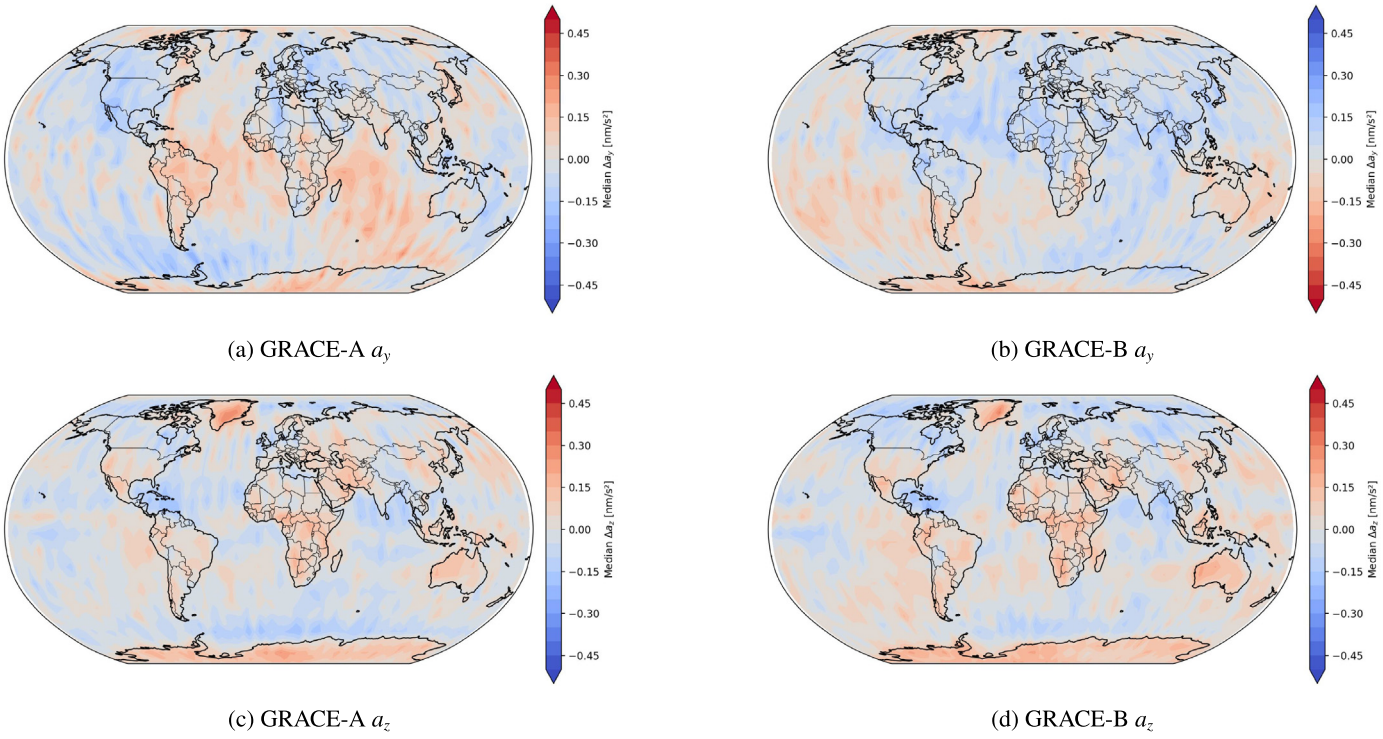

(a) GRACE-A a_y (b) GRACE-B a_y

(c) GRACE-A a_z (d) GRACE-B a_z

Fig. 11. Median residual per 5° by 5° geographical grid cell for GRACE-A (left) and GRACE-B (right) in the cross-track (top) and radial (bottom) direction using a posteriori scale factors and the TY-TZ - extended radiation pressure model.

has been adopted by, e.g., Vielberg and Kusche (2020) based on the work of Su et al. (2015a,b). Findings like this help improve radiation pressure modeling and can be considered in future work.

5.5. Summary of final radiation pressure model and accelerometer calibration parameters

For clarity and convenience, we will now summarize the radiation-pressure model, scale factors, and magnetic-field-induced bias. Therefore, Table 13 shows the proposed thermal model, and Table 14 reports the reflection and absorption coefficients. This work only tuned the accelerometer scale factors using data prior to 2011. In 2011, the accelerometer's thermal control was disabled, resulting in different scale factors. It was observed that the best results are obtained when we scale the cross-track and radial scale factors by the along-track scale factor. The selected scale factors are given in Table 15. Finally, Table 16 gives the coefficients of the magnetic-field-induced bias to be applied to unscaled accelerometer measurements.

6. Effect on crosswind observations from 2003 to 2009

Accelerometer measurements enable in situ observation of crosswinds, providing valuable insights into thermospheric dynamics. Deriving such crosswind observations relies heavily on the accuracy of the aerodynamic acceleration in the cross-track direction, which in turn requires accurate radiation pressure modeling. Thus, we may use crosswind observations to demonstrate improvements in radiation-pressure modeling and to highlight their impact on the existing GRACE crosswind dataset.

To derive crosswind observations from the accelerometer measurements, we use the iterative algorithm described by Doornbos et al. (2010). The crosswind observations require a sufficiently high signal-to-noise ratio in the aerodynamic acceleration. Since the iterative algorithm adjusts the direction of incoming flow, the crosswind that is observed is only approximately aligned with the y-axis. To allow a fair comparison between different sets of observations, we compare only the wind along the satellite y-axis.

The magnitude of aerodynamic acceleration is roughly proportional to atmospheric density, which depends strongly on solar activity and altitude. Solar activity steadily decreased from the maximum in 2002 until the solar minimum in 2008/2009. In the same period, the GRACE satellites' altitude decreased only marginally from about 500 km to 460 km. As a consequence, the magnitude of the aerodynamic acceleration steadily decreased during that period.

On the other hand, radiation pressure depends on the distance to the sun and, therefore, remains relatively constant, largely independent of time and altitude. Thus, the ratio of aerodynamic and radiation pressure acceleration decreased by one order of magnitude in that period (Siemes et al., 2023). Assuming that radiation pressure

Table 13
GRACE thermal radiation panel model proposed in this work. Internal heat generation $P_{gen} = 70W$, heat capacity $C_{body} = 100kJ \cdot K^{-1}$. The values shown in bold were optimized in this work.

Panel	Material	A_j [m^2]	$n_{x,j}$ [–]	$n_{y,j}$ [–]	$n_{z,j}$ [–]	C_j [$J\ K^{-1}$]	k_j [$W\ K^{-1}$]	e_j [–]
Zenith	Solar array	2.1673620	0.0	0.0	−1.0	**8570**	0.10	0.15
Nadir	Teflon	6.0711120	0.0	0.0	1.0	**16585**	0.50	
Port (outer)	Solar array	3.1554792	0.0	−0.766044	−0.642787	**12477**	0.15	0.16
Port (inner)	Kapton (A/A)	0.2282913	0.0	0.766044	0.642787	500	0.10	
Starboard (outer)	Solar array	3.1554792	0.0	0.766044	−0.642787	**12477**	0.15	0.16
Starboard (inner)	Kapton (A/A)	0.2282913	0.0	−0.766044	0.642787	500	0.10	
Front (panel)	Kapton (F/R)	0.9551567	−1.0	0.0	0.0	1000	0.10	
Rear (panel)	Kapton (F/R)	0.9551567	1.0	0.0	0.0	1000	0.10	
Front (antenna)	Kapton (A/A)	0.0461901	0.0	0.0	1.0	400	0.01	
Rear (antenna)	Kapton (A/A)	0.0461901	0.0	0.0	−1.0	400	0.01	
Port (antenna)	Kapton (A/A)	0.0461901	0.0	−1.0	0.0	400	0.01	
Starboard (antenna)	Kapton (A/A)	0.0461901	0.0	1.0	0.0	400	0.01	

Table 14
Absorption and reflection coefficients for GRACE materials proposed in this work. The values shown in bold were optimized in this work.

Panel	$c_{d,vis}$ [–]	$c_{s,vis}$ [–]	$c_{a,vis}$ [–]	$c_{d,ir}$ [–]	$c_{s,ir}$ [–]	$c_{a,ir}$ [–]
Kapton (Apron/Antenna)	**0.08**	**0.88**	**0.04**	0.15	0.23	0.62
Kapton (Front/Rear)	**0.03**	**0.21**	**0.76**	0.15	0.23	0.62
Solar arrays	**0.03**	**0.24**	**0.73**	0.16	0.03	0.81
Teflon	**0.00**	**0.87**	**0.13**	**0.57**	**0.00**	**0.43**

Table 15
Scale factors for the GRACE accelerometer measurements as obtained within this work.

	GRACE-A			GRACE-B		
	S_x [–]	S_y [–]	S_z [–]	S_x [–]	S_y [–]	S_z [–]
2002–2011 (with thermal control)	0.960	0.916	0.879	0.945	0.915	0.878
2011–2017 (without thermal control)	0.936	0.893	0.857	0.928	0.898	0.862

Table 16
Coefficients of the magnetic-field-induced bias (confer Eq. (15)) as to be applied to the non-calibrated accelerometer measurements.

	Linear		Quadratic	
	α_x [$nm\ s^{-2}\mu T^{-1}$]	α_z [$nm\ s^{-2}\mu T^{-1}$]	β_x [$nm\ s^{-2}\mu T^{-2}$]	β_z [$nm\ s^{-2}\mu T^{-2}$]
GRACE-A	1.30×10^{-2}	7.03×10^{-3}	6.91×10^{-4}	3.78×10^{-4}
GRACE-B	2.09×10^{-3}	7.64×10^{-3}	2.74×10^{-4}	2.72×10^{-4}

modeling errors are also relatively constant and dominate the aerodynamic acceleration noise, we conclude that the aerodynamic acceleration's signal-to-noise ratio dropped by one order of magnitude from 2002 to 2009, making GRACE data from that period an ideal showcase for assessing the impact of our extended radiation pressure model on derived crosswinds.

Fig. 12 shows the GRACE-A crosswind observations obtained using the initial radiation pressure model and POD-derived scale factors (initial case), as well as using the tuned radiation pressure model, a posteriori scale factors, and magnetic-field-induced accelerometer bias (TY-TZ - extended case). In both cases, the accelerometer biases in the cross-track and radial directions are calculated using

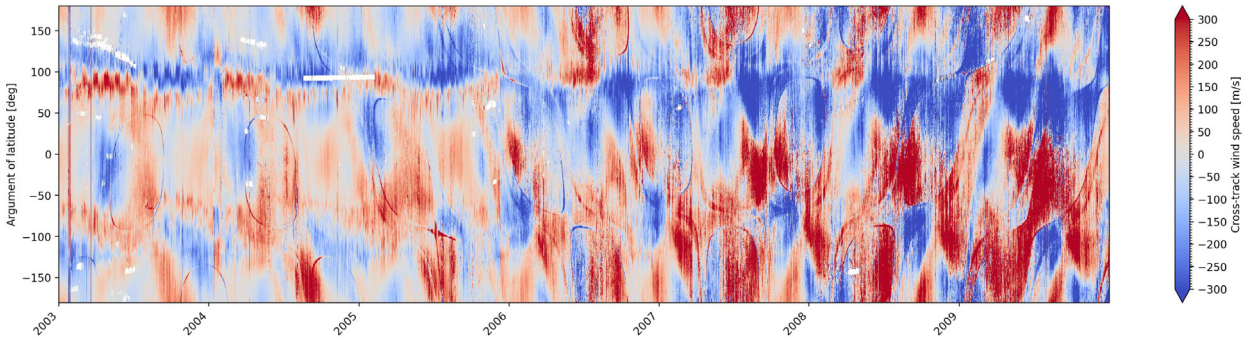

(a) Crosswind observations based on the initial radiation pressure model and POD-derived scale factors (initial case).

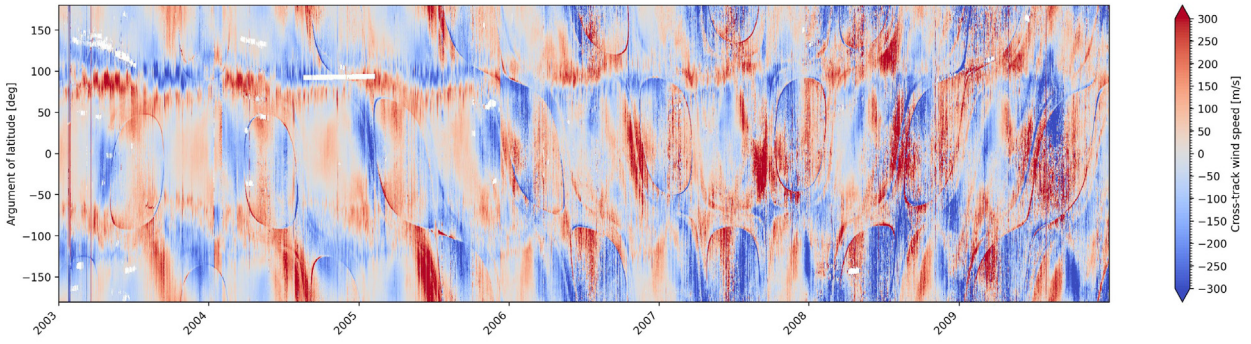

(b) Crosswind observations based on the final radiation pressure model, a posteriori scale factors, and empirical magnetic-field-induced accelerometer bias (TY-TZ - extended case).

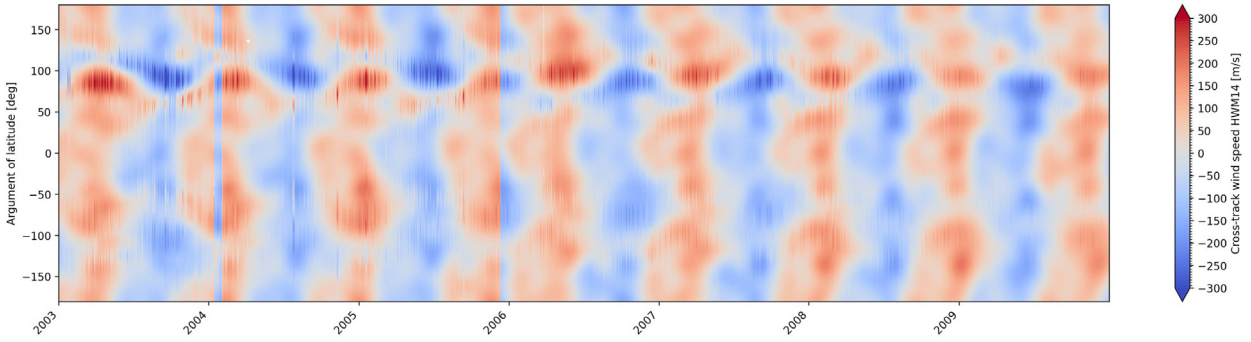

(c) Crosswinds derived from the HWM14.

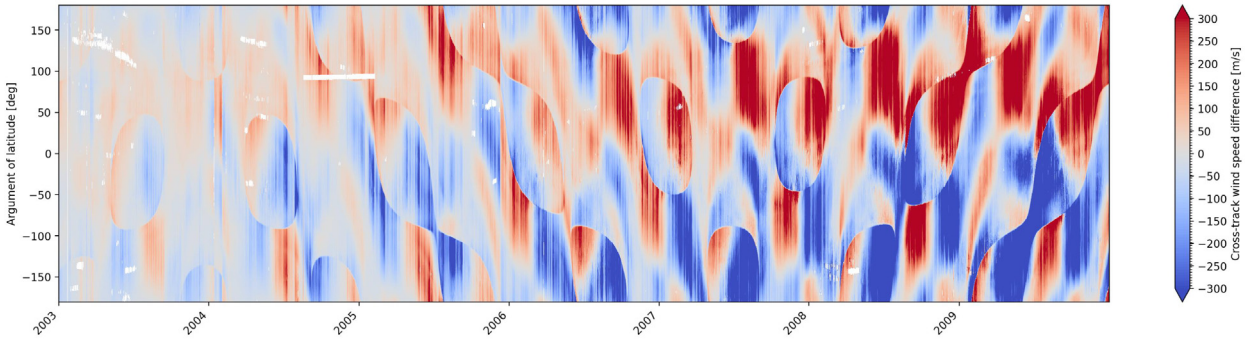

(d) Difference between the two sets of crosswind observations.

Fig. 12. Crosswinds as derived for GRACE-A. From top to bottom: crosswind observations based on the initial radiation pressure model and POD-derived scale factors (initial case), crosswind observations based on the final radiation pressure model, a posteriori scale factors, and magnetic-field-induced accelerometer bias (TY-TZ - extended case), crosswind derived from the HWM14, and the difference between the two sets of crosswind observations.

the obtained non-conservative force models, similar to the method described by Siemes et al. (2023). In the along-track direction, the POD-derived accelerometer bias is used. For reference, the figure also includes crosswinds derived from the HWM14 and the difference between the two sets of crosswind observations.

The two sets of crosswind observations appear very similar in 2003 and the first half of 2004, with differences of tens of m s^{-1} (see bottom panel). Afterward, the differences increase steadily until 2008/2009, when they exceed 300m s^{-1} in many locations. This increase in the difference is clearly due to a strong increase in the derived crosswind in the first dataset generated from the initial case (top panel). The crosswind dataset based on the TY-TZ - extended case does not show such an increase in crosswind speed, although it is evidently noisier from 2006 onward. The crosswind derived from the HWM14 does not increase from 2003 to 2009; if anything, it decreases slightly during that period. Thus, we conclude that the crosswind dataset based on the TY-TZ - extended case is substantially more accurate than that based on the initial case. We also examined the GRACE-B crosswind observations in the same way (not shown), which gave very similar results and led to the exact same conclusion.

7. Summary

This study demonstrates that joint optimization of surface reflection and absorption coefficients, thermal properties, and accelerometer scale factors improves radiation pressure modeling for the GRACE satellites. Focusing on 2009, when solar activity was minimal, and the GRACE satellites' altitude was still relatively high, was key to success.

First, we assessed three optimization cases: no estimation of scale factors during optimization, only estimating the y-axis scale factor, or estimating both the y- and z-axis scale factors. We demonstrated that estimating the y and z-axis scale factors not only reduces the RMS of the residuals the most, but also yields surface properties closest to previously reported values. However, the estimated scale factors are significantly smaller than POD-derived scale factors reported in the literature.

Further, a high consistency between the GRACE-A a priori and a posteriori scale factors enabled the optimization of the GRACE-B scale factor while reusing the surface properties obtained from GRACE-A data, making the method more efficient. When optimizing the surface properties on GRACE-A, the RMS decreased for both GRACE-A and GRACE-B by more than 7% for the y-residuals and 29% for the z-residuals when using a posteriori scale factors.

When analyzing the y-residuals in the geographic domain, we identified a systematic offset that correlates with the magnetic field. Although the cause of this offset remains unexplained and requires further investigation, we were able to model it empirically as a function of the magnetic vector components. Furthermore, the z-residuals showed patterns resembling monthly maps of Earth's infrared emissions, suggesting adjustments to the nadir panel's absorption and reflection coefficients for infrared radiation.

These modifications achieved a reduction of the RMS of more than 5% for both y- and z-residuals with respect to the unmodified TY-TZ case and, remarkably, the difference between GRACE-A and GRACE-B scale factors was only 0.1%. Overall, the TY-TZ - extended case reduced the RMS by more than 13% for the y-residuals and by 32% for the z-residuals compared to the initial case. Additionally, the consistency of the GRACE-A and GRACE-B residuals was significantly improved.

Finally, we examined the impact of the optimized radiation pressure model and scale factors on GRACE crosswind observations from 2003 to 2009. The crosswind observations based on the optimized model remained at sensible wind speeds throughout the entire period, although increased noise perturbed the observation from 2006 to 2009. In contrast, the crosswind observations based on the initial model showed unreasonably high wind speeds from 2006 to 2009, with the strongest wind speeds during the solar minimum in 2008/2009.

8. Outlook

Although the empirical magnetic-field-induced bias significantly improved accuracy, no root cause has been identified to date, but it might be caused by the limited electromagnetic shielding of the accelerometer electronics. Investigating the physical cause of the magnetic-field-induced bias will help us improve our understanding of the instrument and model the given effect more accurately. For GRACE-FO, a preliminary analysis showed no magnetic-field dependence, possibly due to improved shielding of the accelerometer electronics. However, it should be investigated whether other satellites carrying accelerometers, such as CHAMP or Swarm, are also affected.

To further optimize the radiation pressure model, a more elaborate thermal model would be the logical next step. Here, we could also consider including thermal conductivity between the different panels or, even better, transition to a finite element representation of the satellite. Additionally, investigations should be carried out to assess the uncertainties of the tuned parameters. Furthermore, the remaining geographical patterns in the z-residuals suggested the possibility of improving the albedo and/or Earth's infrared emission maps, or refining our assumptions about how sunlight reflects off different surface types. The methods presented in this paper provide a framework for assessing such refinements. Even stronger, they can also be used to assess the non-gravitational force modeling for future satellite missions carrying accelerometers.

Finally, GRACE crosswind observations have been released for the periods from April 2002 to December

2003 and from October 2011 until the end of the mission's science operations in October 2017. Although further analysis of the quality of crosswind observations based on the improvements presented in this paper is needed, previously unreleased crosswind observations, as well as improved versions of those already released, will become available in the future.

Data availability

The GRACE data were downloaded from GFZ's Information System and Data Center (ISDC) data server at https://isdc-data.gfz.de. Aerodynamic force coefficient tables can be retrieved from https://thermosphere.tudelft.nl.

The radiation pressure force coefficient look-up table, calibration coefficients, and density and crosswind data obtained for GRACE-A and GRACE-B over the full mission duration can be found at the 4TU Research Data repository (Jacobs et al., 2026) with 10 s sampling.

Declaration of competing interest

The authors declare that they have no known competing financial interests or personal relationships that could have appeared to influence the work reported in this paper.

Acknowledgments

This publication is part of the project *Relative acceleration modelling (RAM)* with file number *ENW.GO.002.002* of the research programme *Use of space infrastructure for Earth observation and planetary research*, financed by the Dutch Research Council (NWO).

Appendix A. Residual acceleration contour plots

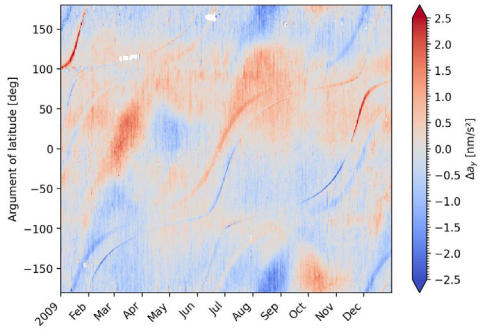

(a) Initial Δa_y

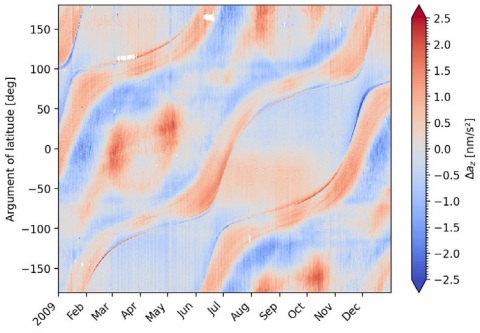

(b) Initial Δa_z

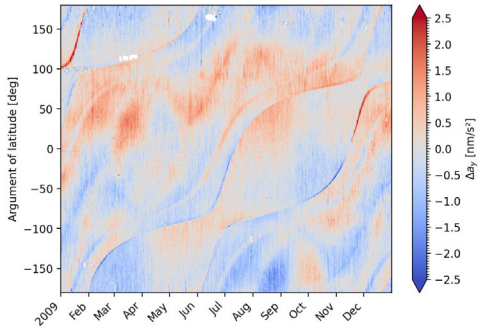

(c) PY-PZ Δa_y

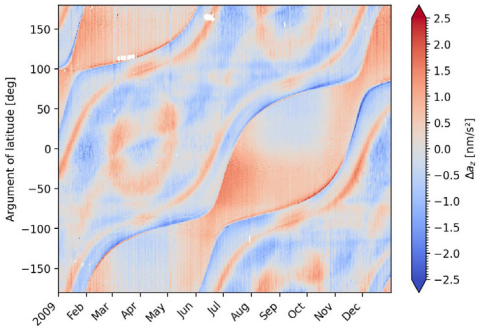

(d) PY-PZ Δa_z

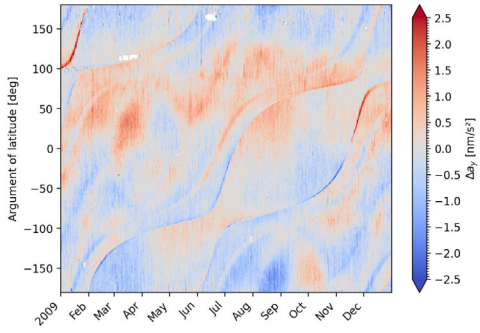

(e) TY-PZ Δa_y

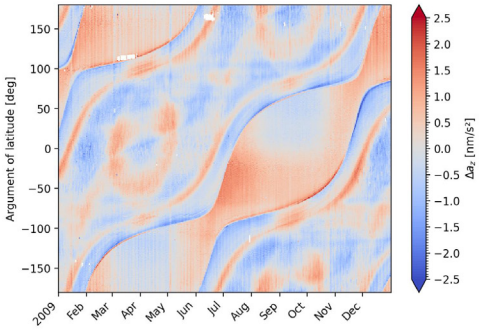

(f) TY-PZ Δa_z

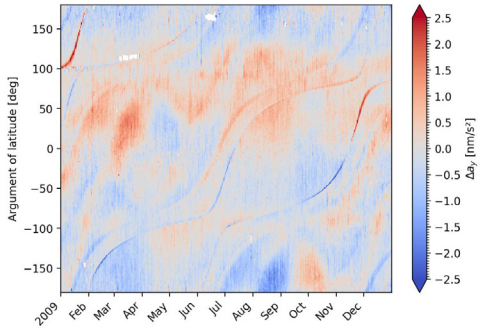

(g) TY-TZ Δa_y

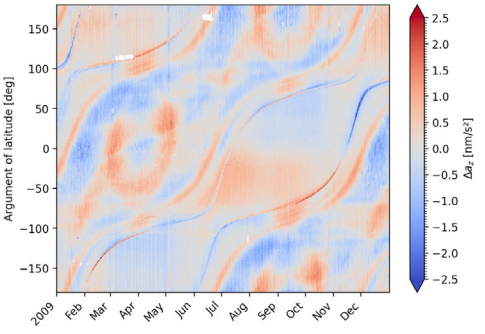

(h) TY-TZ Δa_z

Fig. A1. Residual accelerations for GRACE-A for the different optimization scenarios with a posteriori scaling correction in the y- (left) and the z-direction (right). From top to bottom: initial, PY-PZ, TY-PZ, TY-TZ all with a posteriori scale factors.

Appendix B. Magnetic field measurements

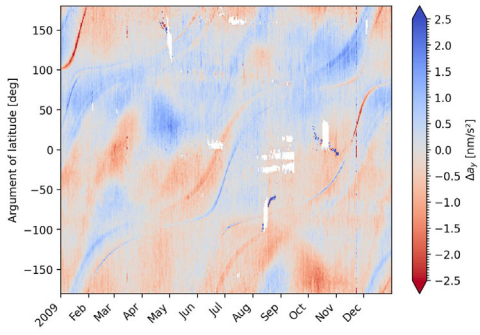

(a) Initial Δa_y

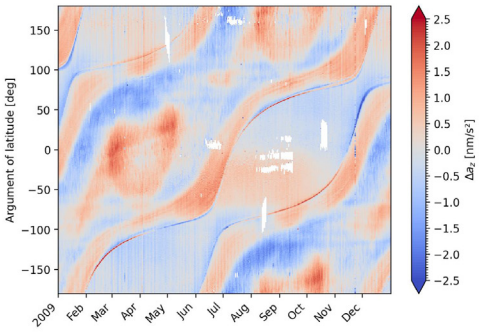

(b) Initial Δa_z

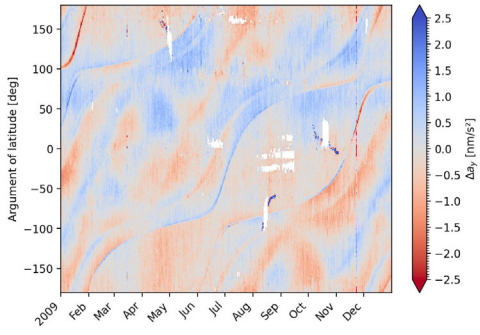

(c) PY-PZ Δa_y

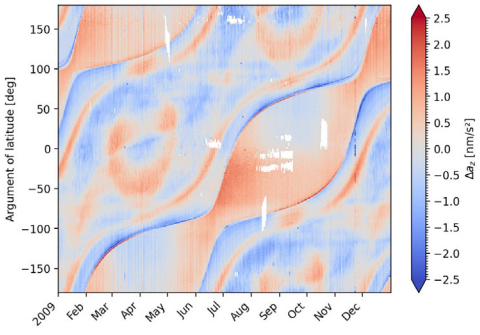

(d) PY-PZ Δa_z

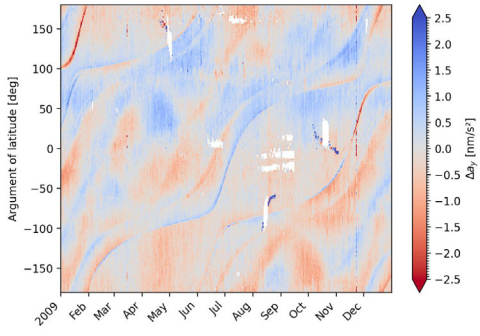

(e) TY-PZ Δa_y

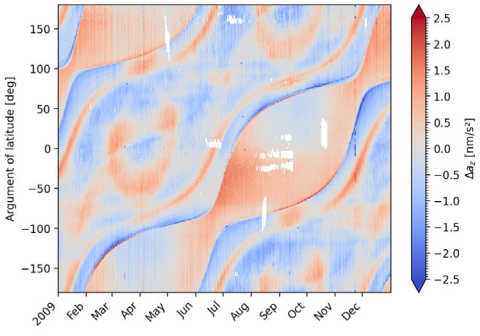

(f) TY-PZ Δa_z

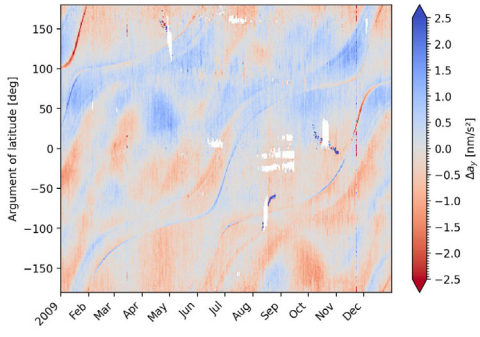

(g) TY-TZ Δa_y

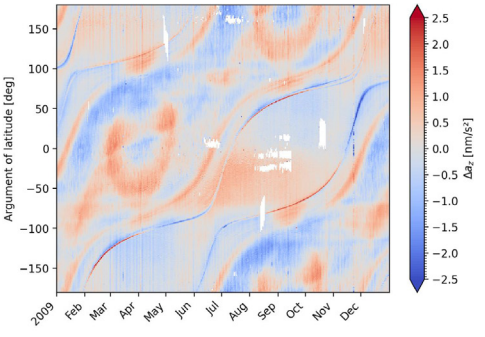

(h) TY-TZ Δa_z

Fig. A2. Residual accelerations for GRACE-B for the different optimization scenarios with a posteriori scaling correction in the y- (left) and the z-direction (right). From top to bottom: initial, PY-PZ, TY-PZ, TY-TZ all with a posteriori scale factors.

Appendix C. Earth albedo and infrared emission maps

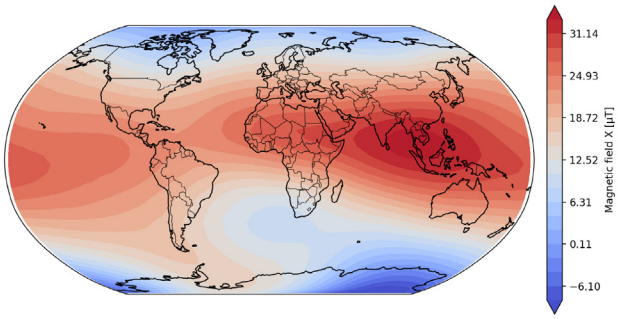

(a) Magnetic vector component B_x

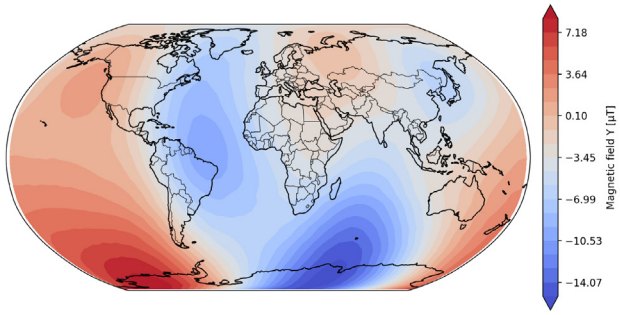

(b) Magnetic vector component B_y

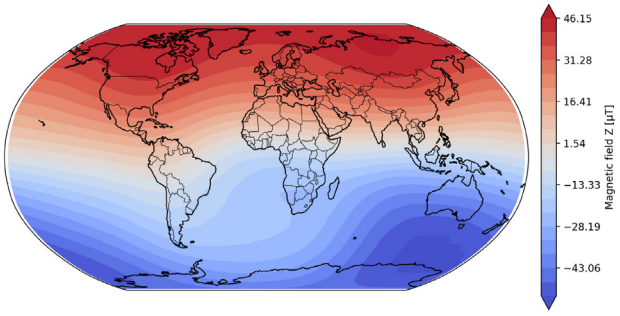

(c) Magnetic vector component B_z

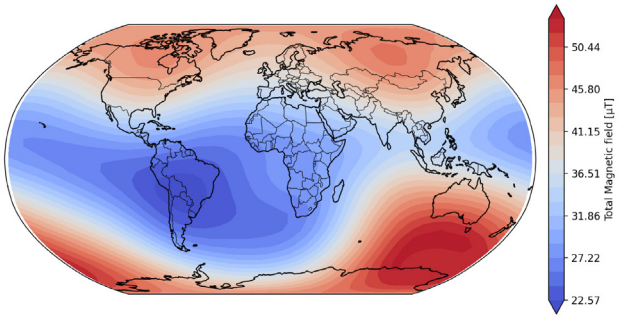

(d) Magnetic field intensity $F = \sqrt{B_x^2 + B_y^2 + B_z^2}$

Fig. A3. Geographical maps of observed magnetic field during ascending tracks for GRACE-A in 2009. Magnetic vector component B_x (top left), B_y (top right), and B_z (bottom left), as well as the magnetic field intensity $F = \sqrt{B_x^2 + B_y^2 + B_z^2}$ (bottom right).

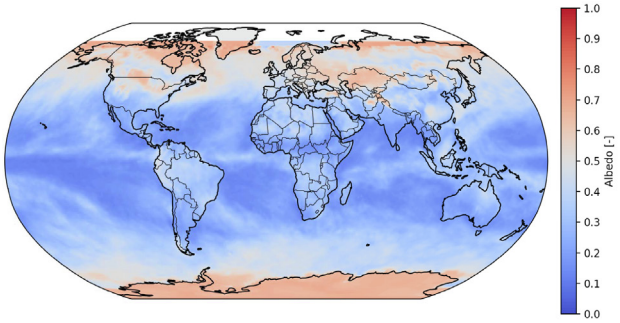

(a) Albedo

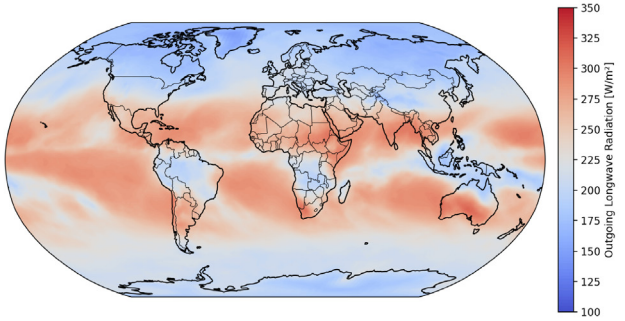

(b) Longwave flux

Fig. A4. Geographical maps of albedo (left) and infrared emission (right) of the Earth in January 2009.

References

Alken, P., Thébault, E., Beggan, C.D., et al., 2021. International geomagnetic reference field: the thirteenth generation. Earth, Planets and Space 73 (1), 49. https://doi.org/10.1186/s40623-020-01288-x.

Bettadpur, S. (2009). Recommendation for A-Priori Bias & Scale Parameters for Level-1B ACC Data (Version 2). GRACE Technical Note 02 NASA.

Bezděk, A., 2010. Calibration of accelerometers aboard GRACE satellites by comparison with POD-based nongravitational accelerations. J. Geodyn. 50 (5), 410–423. https://doi.org/10.1016/j.jog.2010.05.001.

Bruinsma, S., Boniface, C., 2021. The operational and research DTM-2020 thermosphere models. J. Space Weather Space Clim. 11 (47). https://doi.org/10.1051/swsc/2021032.

Bruinsma, S., Sutton, E., Solomon, S.C., et al., 2018. Space weather modeling capabilities assessment: neutral density for orbit determination at low earth orbit. Space Weather 16, 1806–1816. https://doi.org/10.1029/2018SW002027.

Case, K., Kruizinga, G., Wu, S.-C., 2010. GRACE level 1B data product user handbook. Technical Report JPL D-22027 NASA JPL.

Doelling, D.R., Sun, M., Nguyen, L.T., et al., 2016. Advances in geostationary-derived longwave fluxes for the CERES synoptic (SYN1deg) product. J. Atmos. Ocean. Technol. 33 (3), 503–521. https://doi.org/10.1175/JTECH-D-15-0147.1.

Doornbos, E., Den, Van, IJssel, J., Luhr, H., et al., 2010. Neutral density and crosswind determination from arbitrarily oriented multiaxis accelerometers on satellites. J. Spacecr. Rock. 47 (4), 580–589. https://doi.org/10.2514/1.48114.

Drob, D.P., Emmert, J.T., Meriwether, J.W., et al., 2015. An update to the Horizontal Wind Model (HWM): the quiet time thermosphere. Earth and Space Sci. 2 (7), 301–319. https://doi.org/10.1002/2014EA000089.

Emmert, J.T., Jones, M., Siskind, D.E., et al., 2022. NRLMSIS 2.1: an empirical model of nitric oxide incorporated into MSIS. J. Geophys. Res.: Space Phys. 127 (10). https://doi.org/10.1029/2022JA030896, e2022JA030896.

Harvey, N., Sakumura, C., 2019. Results from a GRACE/GRACE-FO attitude reconstruction Kalman filter. J. Geodesy 93 (10), 1881–1896. https://doi.org/10.1007/s00190-019-01289-z.

Helleputte, T.V., Doornbos, E., Visser, P., 2009. CHAMP and GRACE accelerometer calibration by GPS-based orbit determination. Adv. Space Res. 43 (12), 1890–1896. https://doi.org/10.1016/j.asr.2009.02.017.

Hładczuk, N., Den, Van, IJssel, J., Kodikara, T., et al., 2024. Grace-fo radiation pressure modelling for accurate density and crosswind retrieval. Adv. Space Res. 73 (5), 2355–2373. https://doi.org/10.1016/j.asr.2023.12.059.

Jacobs, F., Hładczuk, N., Van Den IJssel, J. et al., 2026. Data supporting the article "Joint optimization of a GRACE radiation pressure model, the accelerometer scale factors, and an empirical magnetic-field-induced accelerometer bias". https://doi.org/10.4121/5bfa73b6-8e6a-45da-8a96-110fe0518aed.

Koch, I., Shabanloui, A., Flury, J., 2018. Calibration of GRACE accelerometers using two types of reference accelerations. In: Freymueller, J.T., Sánchez, L. (Eds.), International Symposium on Advancing Geodesy in a Changing World, volume 149. Springer International Publishing, Cham, pp. 97–104. https://doi.org/10.1007/1345_2018_46.

Kornfeld, R.P., Arnold, B.W., Gross, M.A., et al., 2019. GRACE-FO: the gravity recovery and climate experiment follow-on mission. J. Spacecr. Rock. 56 (3), 931–951. https://doi.org/10.2514/1.A34326.

Loeb, N.G., Wielicki, B.A., Doelling, D.R., et al., 2009. Toward optimal closure of the Earth's top-of-atmosphere radiation budget. J. Clim. 22 (3), 748–766. https://doi.org/10.1175/2008JCLI2637.1.

March, G., Doornbos, E., Visser, P., 2019. High-fidelity geometry models for improving the consistency of CHAMP, GRACE, GOCE and Swarm thermospheric density data sets. Adv. Space Res. 63 (1), 213–238. https://doi.org/10.1016/j.asr.2018.07.009.

Montenbruck, O., Gill, E., 2000. Satellite Orbits. Berlin, Heidelberg: Springer, Berlin Heidelberg. URL: http://link.springer.com/10.1007/978-3-642-58351-3. doi:10.1007/978-3-642-58351-3.

Robertson, R., Flury, J., Bandikova, T., et al., 2015. Highly physical penumbra solar radiation pressure modeling with atmospheric effects. Celest. Mech. Dynam. Astron. 123 (2), 169–202. https://doi.org/10.1007/s10569-015-9637-0.

Siemes, C., Borries, C., Bruinsma, S., et al., 2023. New thermosphere neutral mass density and crosswind datasets from CHAMP, GRACE, and GRACE-FO. J. Space Weather Space Clim. 13, 16. https://doi.org/10.1051/swsc/2023014.

Su, W., Corbett, J., Eitzen, Z., et al., 2015a. Next-generation angular distribution models for top-of-atmosphere radiative flux calculation from CERES instruments: Methodology. Atmos. Meas. Tech. 8 (2), 611–632. https://doi.org/10.5194/amt-8-611-2015.

Su, W., Corbett, J., Eitzen, Z., et al., 2015b. Next-generation angular distribution models for top-of-atmosphere radiative flux calculation from CERES instruments: Validation. Atmos. Meas. Tech. 8 (8), 3297–3313. https://doi.org/10.5194/amt-8-3297-2015.

Tapley, B.D., Bettadpur, S., Watkins, M., et al., 2004. The gravity recovery and climate experiment: Mission overview and early results. Geophys. Res. Lett. 31 (9). https://doi.org/10.1029/2004GL019920, 2004GL019920.

Teixeira Da Encarnação, J., Save, H., Tapley, B., et al., 2020. Accelerometer parameterization and the quality of gravity recovery and climate experiment solutions. J. Spacecr. Rock. 57 (4), 740–752. https://doi.org/10.2514/1.A34639.

Touboul, P., Foulon, B., Christophe, B. et al. (2012). CHAMP, GRACE, GOCE Instruments and Beyond. In S. Kenyon, M.C. Pacino, & U. Marti (Eds.), Geodesy for Planet Earth (pp. 215–221). Berlin, Heidelberg: Springer, Berlin Heidelberg volume 136. doi:10.1007/978-3-642-20338-1_26.

Vielberg, K., Forootan, E., Lück, C., et al., 2018. Comparison of accelerometer data calibration methods used in thermospheric neutral density estimation. Ann. Geophys. 36 (3), 761–779. https://doi.org/10.5194/angeo-36-761-2018.

Vielberg, K., Kusche, J., 2020. Extended forward and inverse modeling of radiation pressure accelerations for LEO satellites. J. Geodesy 94 (4), 43. https://doi.org/10.1007/s00190-020-01368-6.

Wang, C., Yu, W., Bai, Y., et al., 2025. Theoretical modeling and experimental investigation of magnetic field multiplicative coupling of differential transformers in space inertial sensors. Meas. Sci. Technol. 36 (5), 055018. https://doi.org/10.1088/1361-6501/add361.

Wang, F., 2003. Study on center of mass calibration and K-brand ranging system calibration of the GRACE mission PhD thesis. The University of Texas at Austin.

Wen, H.Y., Kruizinga, G., Paik, M. et al., 2019. Gravity Recovery and Climate Experiment Follow-On (GRACE-FO) Level-1 Data Product User Handbook. Technical Report JPL D-56935 (URS270772) NASA JPL.

Wöske, F., Huckfeldt, M., Rievers, B., 2024. Tailored accelerometer calibration by POD for thermospheric density retrieval with GRACE and GRACE-FO. Adv. Space Res. 74 (10), 4517–4542. https://doi.org/10.1016/j.asr.2024.09.021.

Wöske, F., Kato, T., Rievers, B., et al., 2019. GRACE accelerometer calibration by high precision non-gravitational force modeling. Adv. Space Res. 63 (3), 1318–1335. https://doi.org/10.1016/j.asr.2018.10.025.